

An Abstract of the Thesis of

Keone R. Streicher for the degree of Master of Science in Electrical and Computer Engineering presented on July 12, 1994.

Title: Electro-Optic Characterization of ZnS:Tb ACTFEL Devices for Probing the Hot Electron Distribution

Abstract approved: Redacted for Privacy
Dr. Thomas K. Plant

In this report, the optical characteristics of ZnS:Tb AC driven thin-film electroluminescent devices are evaluated. Luminescence at low and room temperature under a constant phosphor field is recorded in order to probe the hot electron energy distribution. Samples fabricated by atomic layer epitaxy and by sputter deposition are investigated and their differences and similarities evaluated. The ALE sample exhibits a drastic increase in luminescence at low temperature, while the sputtered sample displays a decrease in luminescence at low temperature. The reduction of optical phonon scattering and nonradiative transition rates at low temperature are believed to be responsible for these changes. Differences between ALE and sputtered samples are due to the different fabrication methods. The approach suggested by Krupka in 1972 of determining the hot electron energy distribution by taking the ratio intensities of two luminescent transitions from different upper states in Tb^{3+} , is shown to be inaccurate due to the possible nonradiative transitions taking place. The Tb^{3+} impact excitation quantum yield at a wavelength of 489 nm is measured and is shown to agree with Monte Carlo simulations. Saturation occurs due to the increase in band-to-band impact ionization at high phosphor fields.

**Electro-Optic Characterization of ZnS:Tb ACTFEL Devices
for Probing the Hot Electron Distribution**

by

Keone R. Streicher

**A THESIS
submitted to
Oregon State University**

**in partial fulfillment of
the requirements for the
degree of**

Master of Science

Completed July 12, 1994

Commencement June 1995

Approved:

Redacted for Privacy

Associate Professor of Electrical & Computer Engineering in charge of major

Redacted for Privacy

Head of Department of Electrical & Computer Engineering

Redacted for Privacy

Dean of Graduate School

Date thesis is presented: July 12, 1994.

Typed by Keone R. Streicher.

Acknowledgements

I would like to thank my advisor, Dr. Thomas K. Plant, for his continued support, advice and encouragement during the last two years.

I would also like to thank Professors John F. Wager for his advice and enlightening discussions, S. M. Goodnick, and Milo Koretsky for serving on my committee.

Special thanks to Wie Ming Ang, Shankar Pennathur, and Robert Thuemmler for many useful discussions.

In addition, I would like to thank Ron Khormaei, Chris King and Dick Tuenge of Planar Systems for providing samples used throughout this research.

Furthermore, I wish to acknowledge David Morton, Chris Hogh, and James Koh of the U.S. Army LABCOM for the use of their laboratory and for offering their expertise.

This work was supported by the Advanced Research Projects Agency under the Phosphor Technology Center of Excellence, Grant No. MDA 972-93-1-0030.

Table of Contents

1.0	Introduction	1
2.0	Tb³⁺-Doped Thin-Film Electroluminescent Device Operation: Literature Review	4
2.1	Device Structure	4
2.2	Device Fabrication	5
2.3	Summary of Physics of Operation	6
2.4	Electrical Measurement Techniques	10
2.5	Electron Transport	16
2.6	Tb ³⁺ Energy Levels and ZnS Crystal Lattice Interaction	17
2.7	Review of Experiments Conducted on ZnS:Tb	25
3.0	Experimental Setup for Luminescence Measurements	27
3.1	Introduction	27
3.2	Experimental Setup	29
3.2.1	Diagram of the Field-Control Circuit	32
3.2.2	Optical Setup and Measurement Techniques	34
4.0	Hot Electron Luminescence	37
4.1	Introduction	37
4.2	Standard Waveform Experiments	38
4.2.1	Room and Low Temperature Experimental Results	38
4.2.2	Discussion and Summary	45
4.3	Field-Control Waveform Experiments	46
4.3.1	Room and Low Temperature Experimental Results	46
4.3.2	Discussion and Summary	70
5.0	Conclusions/Recommendations	74
5.1	Conclusions	74
5.2	Future Work	74
	Bibliography	78

List of Figures

Figure 2-1.	Typical TFEL device structure	5
Figure 2-2.	Standard voltage waveform	6
Figure 2-3.	Energy band diagram; no external bias applied	7
Figure 2-4.	Energy band diagram; positive external bias applied to the Al electrode	7
Figure 2-5.	Energy band diagram; polarization charge after positive pulse	8
Figure 2-6.	Energy band diagram; negative external bias applied to the Al electrode	9
Figure 2-7.	Energy band diagram; polarization charge after negative pulse	10
Figure 2-8.	C-V curve for ZnS:Tb	12
Figure 2-9.	Q-V curve for ZnS:Tb	13
Figure 2-10.	Q-F _p curve for ZnS:Tb	15
Figure 2-11.	Experimental setup for electrical measurements	16
Figure 2-12.	Examples of possible total angular momentum for the ground state of Tb ³⁺	20
Figure 2-13.	Energy level diagram of Tb ³⁺	22
Figure 2-14a.	Optical spectrum of ZnS:Tb from 360 nm to 475 nm. Vertical scale is 100x expanded from Fig. 2-14b	24
Figure 2-14b.	Optical spectrum of ZnS:Tb from 475 nm to 675 nm	25
Figure 3-1.	Standard voltage waveform	29
Figure 3-2.	Driving waveform including the field-control pulse	29
Figure 3-3.	Field-control experimental setup	31

Figure 3-4.	Diagram of the field-control circuit	33
Figure 3-5.	Optical setup	35
Figure 4-1.	Trapezoidal voltage pulse and luminescence at 543 nm	39
Figure 4-2.	Intensity at 437nm at T=295 K and T=147 K for the ALE sample	39
Figure 4-3.	Intensity at 489nm at T=295 K and T=147 K for the ALE sample	40
Figure 4-4.	Intensity at 543nm at T=295 K and T=147 K for the ALE sample	40
Figure 4-5.	Intensity at 437 nm at T=295 K and T=113 K for the sputtered sample	41
Figure 4-6.	Intensity at 489 nm at T=295 K and T=113 K for the sputtered sample	42
Figure 4-7.	Intensity at 543 nm at T=295 K and T=113 K for the sputtered sample	42
Figure 4-8.	Ratio $I(437\text{ nm})/I(489\text{ nm})$ at T=295 K and T=147 K for the ALE sample	44
Figure 4-9.	Ratio of $I(437\text{ nm})/I(489\text{ nm})$ at T=295 K and T=113 K for the sputtered sample	44
Figure 4-10.	Field-control waveform and corresponding luminescence at 543 nm	46
Figure 4-11.	Example of a field-control pulse	48
Figure 4-12.	Phosphor fields at T=295 K for the ALE sample	49
Figure 4-13.	Phosphor fields at T=147 K for the ALE sample	49
Figure 4-14.	Phosphor fields at T=295 K for the sputtered sample	51
Figure 4-15.	Phosphor fields at T=113 K for the sputtered sample	51
Figure 4-16.	Internal charge at T=295 K for the ALE sample	53
Figure 4-17.	Internal charge at T=147 K for the ALE sample	54

Figure 4-18.	Internal charge at T=295 K for the sputtered sample	55
Figure 4-19.	Internal charge at T=113 K for the sputtered sample	55
Figure 4-20.	Q-Fp curves at T=295 K for the ALE sample	56
Figure 4-21.	Q-Fp curves at T=147 K for the ALE sample	57
Figure 4-22.	Q-Fp curves at T=295 K for the sputtered sample	57
Figure 4-23.	Q-Fp curves at T=113 K for the sputtered sample	58
Figure 4-24.	Internal charge $q(t)$ versus time with variations in C_p	60
Figure 4-25.	Q-F _p with variations in C_p	60
Figure 4-26.	Intensity at 437 nm for T=295 K and T=147 K for the ALE sample	61
Figure 4-27.	Intensity at 489 nm for T=295 K and T=147 K for the ALE sample	62
Figure 4-28.	Intensity at 543 nm for T=295 K and T=147 K for the ALE sample	62
Figure 4-29.	Intensity at 437 nm for T=295 K and T=113 K for the sputtered sample	63
Figure 4-30.	Intensity at 489 nm for T=295 K and T=113 K for the sputtered sample	63
Figure 4-31.	Intensity at 543 nm for T=295 K and T=113 K for the sputtered sample	64
Figure 4-32.	Ratio of $I(437 \text{ nm})/I(489 \text{ nm})$ for T=295 K and T=147 K for the ALE sample	65
Figure 4-33.	Ratio of $I(437 \text{ nm})/I(489 \text{ nm})$ for T=295 K and T=113 K for the sputtered sample	65
Figure 4-34.	Normalized intensity at 489 nm for T=295 K and T=147 K for the ALE sample	66
Figure 4-35.	Normalized intensity at 489 nm for T=295 K and T=113 K for the sputtered sample	67

Figure 4-36. Normalized intensity at 489 nm for the ALE and the sputtered sample 68

Figure 4-37. Internal quantum yield for terbium impact excitation and ionization as a function of the phosphor field in ZnS:Tb 69

List of Tables

Table 2-1	Transitions of Tb^{3+} with and without crystal field splitting	23
Table 3-1	Current amplification of the 928 Hamamatsu PMT	36
Table 4-1	Parameters for ALE sample	47
Table 4-2	Parameters for sputtered sample	47
Table 4-3	Conversion from applied voltage to phosphor field in the ALE sample	50
Table 4-4	Conversion from applied voltage to phosphor field in the sputtered sample	52

Electro-Optic Characterization of ZnS:Tb ACTFEL Devices for Probing the Hot Electron Distribution

1.0 Introduction

In today's information age the need for new video display technology is rising drastically. The trend is to move away from conventional bulky displays such as cathode ray tubes (CRT) and toward the more compact flat panel and heads-up displays. The leading technologies for flat panel displays are liquid crystal (LCD), plasma, field emission, and electroluminescent displays (EL).

Liquid crystal displays use a white light source to illuminate the display where the color of each pixel is controlled by the voltage applied across it. Plasma displays use the UV luminescence from a gas discharge to excite phosphors. Field emission displays use electrons emitted from an array of point emitters and accelerated across a small gap to impact excite a phosphor layer. Electroluminescent displays are solid state devices which are fabricated using thin film technology and convert electrical energy into luminous energy by electron impact excitation of the phosphor.

At the moment liquid crystal displays are dominating the flat panel display market. There is a multi-billion dollar investment in these displays. Electroluminescent displays make up only a small fraction of the world market. The main reason for this is the difficulty of creating a full-color EL display.

There are some distinct advantages of electroluminescent displays over LCD's. Ruggedness and temperature-independence are the most important factors why the military and commercial airline industries are interested in this technology. EL devices are also emissive displays which are brighter than LCD's and viewable from large angles. This makes them very desirable for heads-up displays.

There are two types of electroluminescent displays, dc and ac driven. Alternating-current thin-film electroluminescent (ACTFEL) displays are preferred because of suitable matrix addressing schemes and present solid-state processing technology. The performance of dc driven EL displays deteriorates with time making them unsuitable for displays. There are problems involved in generating EL flat panel displays. For one, the fabrication process is very critical to the performance of the display. Some of the fabrication methods are evaporation, rf sputtering, and more recently, atomic layer epitaxy (ALE).

Another problem which needs to be solved is the generation of intense blue emission. Presently the red color is achieved by using a color filter in front of the manganese-doped zinc sulfide (ZnS:Mn) phosphor. ZnS:Mn generates yellowish-orange light. The green color is obtained by using the ZnS:Tb phosphor. Blue emission still poses a problem. ZnS:Tm,F and SrS:Ce phosphors give a good blue emission but the brightness is not satisfactory. The efficiency needs to be increased so that a full-color display can be generated. Some drastic breakthroughs have been accomplished recently. Last year the first full-color EL display was achieved. A high resolution heads-up display has also been successfully demonstrated.

It is important to understand the electrical characteristics as well as the underlying physics of these devices and the exact electron distribution inside these devices. Direct electron impact excitation has been established as the dominant mechanism for luminescence; however, there is some controversy regarding the electron transport mechanisms. These issues need to be solved in order to be able to generate an accurate model for successful simulation of the device behavior and to assess whether or not the efficiency can be improved.

The main goals of this thesis are to take measurements to help assess the electron energy distribution in the green ZnS:Tb phosphor and to determine the electron impact excitation efficiency. Electrons accelerated by the high field in the phosphor strike the

rare-earth impurities and excite these ions into a higher state. The ion relaxes into its ground state while giving off photons of characteristic wavelength. By studying the light emitted by the different transitions, we try to assess the hot electron energy distribution, and thus we can determine what fraction of the electrons have energies large enough to contribute directly toward luminescence. We can also measure the excitation efficiency of the electrons to help assess overall device performance.

Chapter 2 reviews relevant literature about the fundamental device physics of the green ZnS:Tb ACTFEL device, including electrical characterization techniques and a review of research conducted on ZnS:Tb. Chapter 3 shows in detail the setup of the experiments and the preparations for taking accurate spectral measurements. It also includes the optical setup and measurements techniques. Chapter 4 discusses and compares the results obtained from ALE and sputter deposited samples at room and low temperature. Chapter 5 presents conclusions and recommendations for future research.

2.0 Tb³⁺-doped Thin-Film Electroluminescent Device Operation Literature Review

In this chapter relevant literature is reviewed, including techniques for electrical measurements. The origin of the terbium ion (Tb³⁺) energy levels and crystal lattice interaction are discussed. The chapter concludes with a short review of the research conducted on zinc sulfide doped with the rare earth metal terbium (ZnS:Tb).

2.1 Device Structure

Thin film electroluminescent (TFEL) devices are processed in a stacked layer configuration. The typical structure of a TFEL device is shown in Fig. 2-1. The substrate of this structure is glass. The upper electrode is generally aluminum and the lower electrode is a transparent conductor, usually indium tin oxide (ITO). The phosphor layer is sandwiched between two insulating layers which have a high electric breakdown voltage and high dielectric constant. This ensures that there is no current leakage through these layers and that most of the external voltage applied to the stack drops across the phosphor layer, and not the insulators. The phosphor layer consists of ZnS, a II-VI type semiconductor, doped with either the rare earth metal terbium (Tb) or terbium oxyfluoride (TbO_xF_y). The newest configuration of TFEL devices are stacked on silicon which incorporates the driving circuitry for the display device.

2.2 Device Fabrication

The devices used in the following experiments are samples fabricated by Planar Systems, Inc., of Beaverton, Oregon, using ALE or RF-sputtering. Both types of samples are annealed using rapid thermal annealing (RTA). The sputtered devices use barium tantalate (BTO) as insulating layers while the ALE samples use aluminum titanium oxide (ATO) insulator layers. The glass substrate is 7059 Corning glass. The back electrode is made of aluminum and the transparent electrode is ITO. The phosphor layer is ZnS doped with the rare earth metal terbium (Tb) in the ALE material and terbium oxyfluoride (TbO_xF_y) in the sputtered samples.

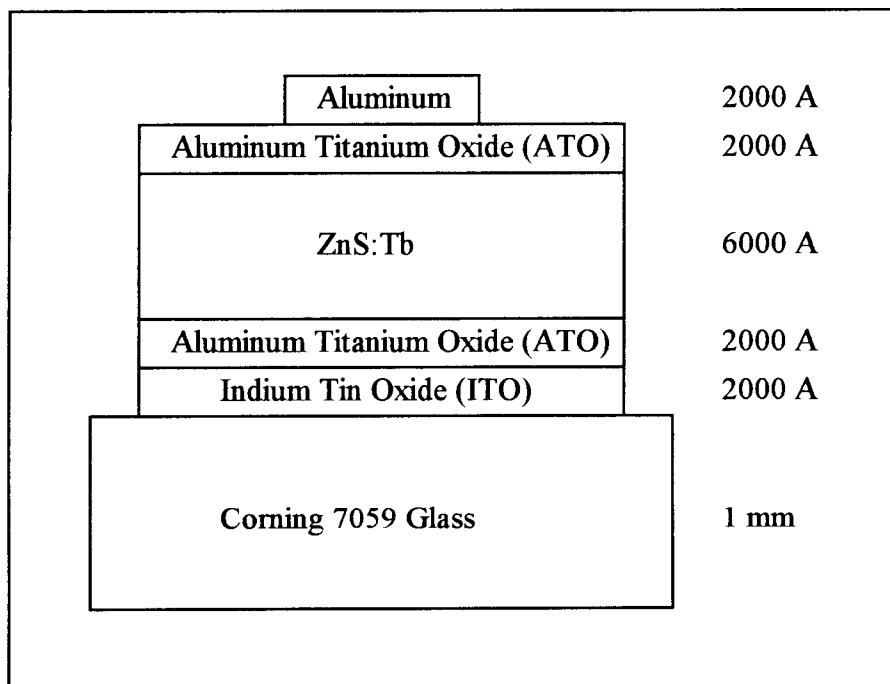


Figure 2-1. Typical TFEL device structure.

2.3 Summary of the Physics of Operation

An ACTFEL device emits light if a succession of large voltage pulses with alternating polarities is applied across its terminals. The form of the waveform is generally a high voltage trapezoid with short rise and fall times and a small duty cycle (less than 1 %). The pulse rise and fall times are 5 μ s and the peak voltage 30 μ s duration and the repetition rate varies from 100 Hz to 10 kHz. The maximum applied voltage is generally 30 V to 80 V above the threshold voltage of the device. For the Tb-doped samples the threshold voltage lies around 160 V, therefore the maximum applied voltage is around 240 V. Fig. 2-2 shows the general waveform of the applied voltage.

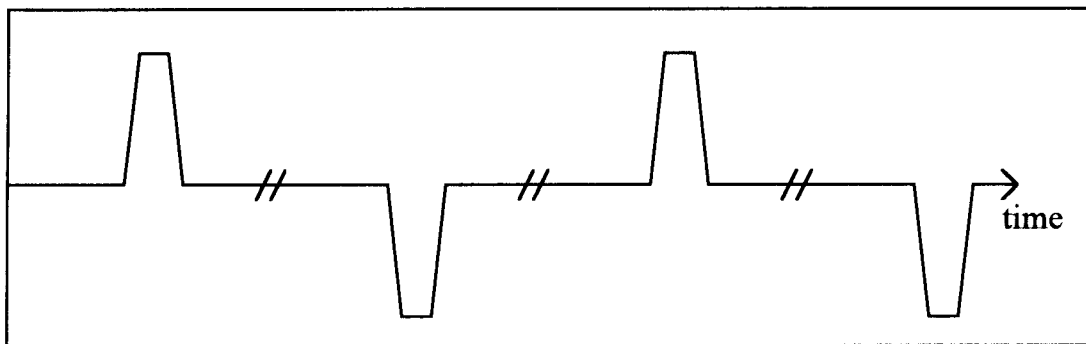


Figure 2-2. Standard voltage waveform.

The energy band diagram for this device with no external applied bias is shown in Fig. 2-3.

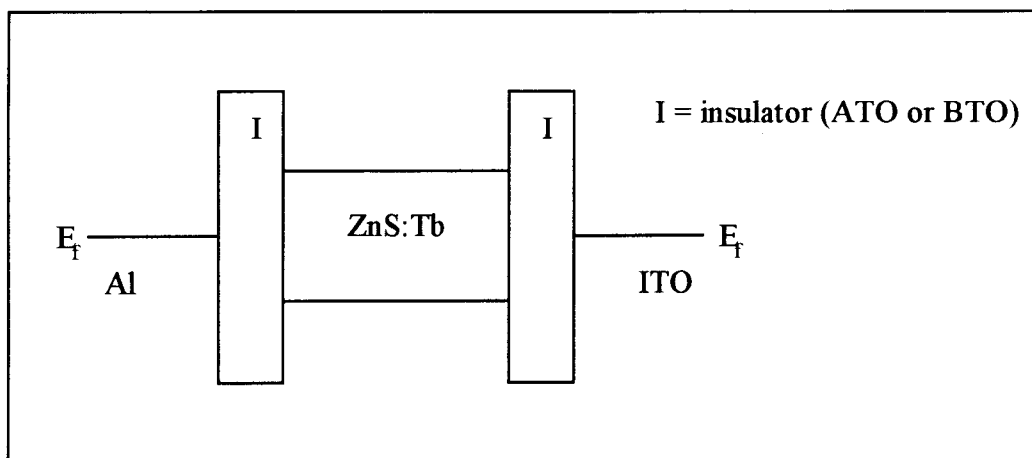


Figure 2-3. Energy band diagram; no external bias applied.

Fig. 2-4 shows the band diagram when a positive pulse is applied to the Al electrode. When the voltage across the phosphor reaches a critical value, which

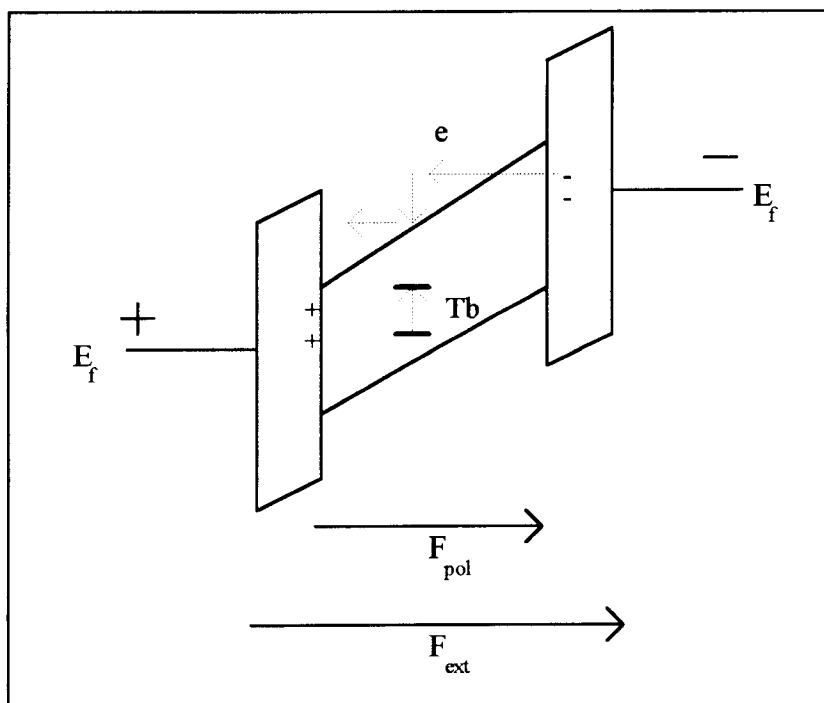


Figure 2-4. Energy band diagram; positive external bias applied to the Al electrode.

corresponds to the externally applied threshold voltage, electrons tunnel from the insulator/ZnS interface states into the ZnS conduction band. This is seen in a sharp increase in conduction current. The high field present in the phosphor due to the applied voltage accelerates the electrons toward the opposite phosphor/insulator interface.

During their travel to the other side, some of the electrons collide with luminescent centers, thus losing some of their kinetic energy to them. If the energy of the electrons is high enough as they strike the impurity, the luminescent centers will jump into an excited state and then decay, giving off photons of characteristic wavelength. The emitted light from the Tb ion is dominated by a sharp peak centered around 542nm which corresponds to a green color.

The electrons continue their path toward the other phosphor side and are trapped at interface states. Since all the electrons now reside on one side of the phosphor, a charge imbalance is present within the phosphor. The emitting interface is now positively charged while the collecting interface is now negatively charged. This buildup of charge after the voltage pulse has subsided is called polarization charge (see Fig. 2-5).

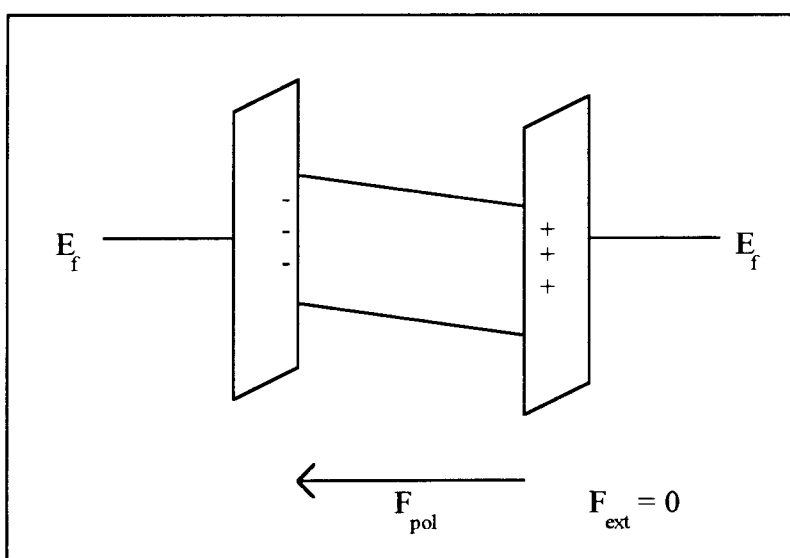


Figure 2-5. Energy band diagram; polarization charge after positive pulse.

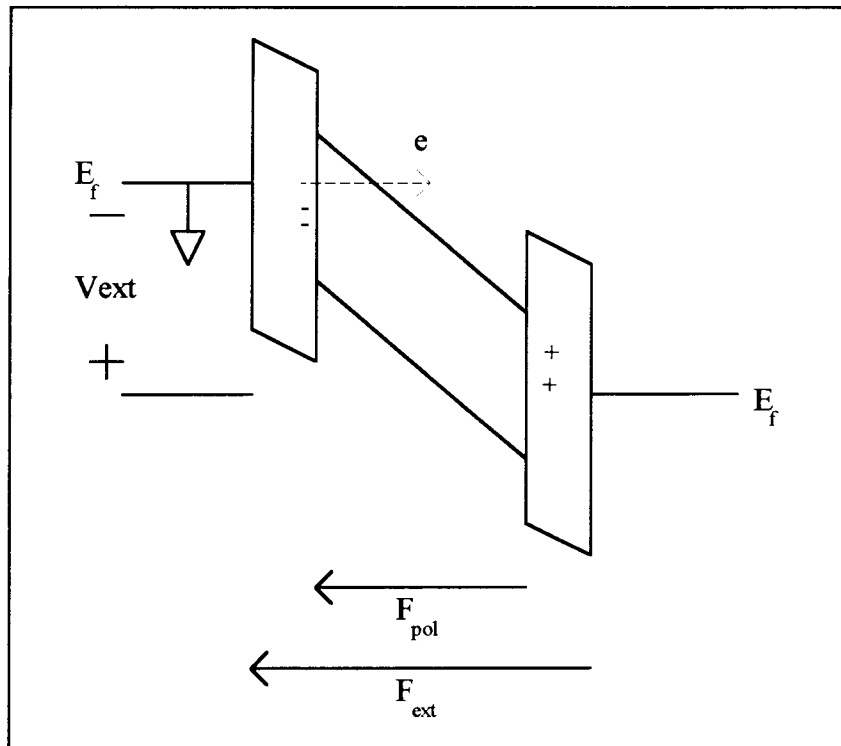


Figure 2-6. Energy band diagram; negative external bias applied to the Al electrode.

When a pulse of opposite polarity is applied, the same process takes place again except that the polarization charge from the previous pulse aids in the emission of electrons (see Fig. 2-6). The threshold voltage for this pulse is therefore lowered due to the field created by the polarization charge.

The voltage which needs to be applied to the device is now lower than the initial threshold voltage and is called the turn-on voltage. The electrons move toward the other insulator/phosphor interface while impact-exciting luminescent centers. At the end of this pulse, a polarization charge of opposite polarity is seen because the electrons now reside at the other insulator/phosphor interface (see Fig. 2-7). This process continues and steady state is reached after a few cycles.

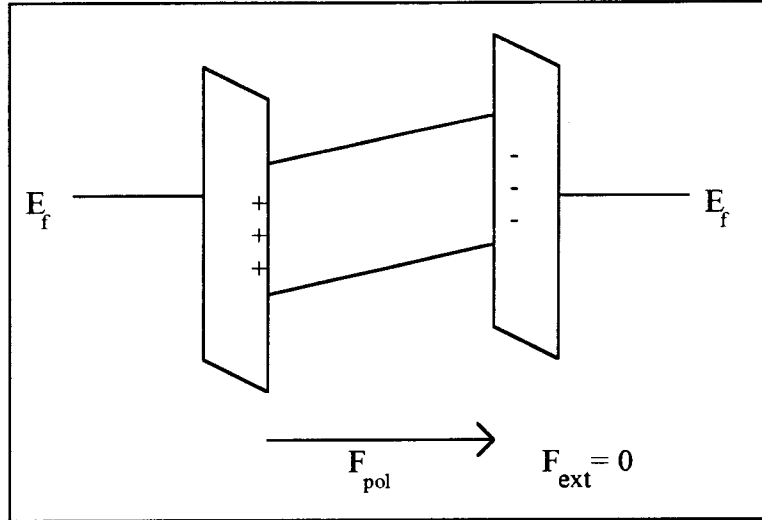


Figure 2-7. Energy band diagram; polarization charge after negative pulse.

2.4 Electrical Measurement Techniques

When assessing the electrical performance of these devices it is important to know the amount of charge being transferred within the phosphor. Information about the internal device physics can be obtained by capacitance-voltage (C-V), charge-voltage (Q-V), and internal charge-phosphor field ($Q - F_p$) methods, which are explained in more detail later. In all cases only the external applied voltage, the current through the device, and the voltage across the sense device (Sawyer-Tower capacitor or resistor) [1] need to be known as functions of time.

The C-V [2-5] measures only external device quantities. Here the capacitance of the stack is given by

$$C = \frac{i(t)}{\frac{dV(t)}{dt}} \quad (2-1)$$

where $i(t)$ is the current through the device and $V(t)$ the voltage across the device.

$$V(t) = V_{\text{ext}}(t) - V_{\text{st}}(t) \quad (2-2)$$

$V_{\text{ext}}(t)$ is the externally applied voltage and $V_{\text{st}}(t)$ is the voltage across the sensing device (in this case a resistor). The current $i(t)$ can be found by dividing $V_{\text{st}}(t)$ by the resistance R_{st} .

$$i(t) = \frac{V_{\text{st}}(t)}{R_{\text{st}}} \quad (2-3)$$

The C-V graph provides information on the insulator and total capacitance of the device. Below threshold the capacitance measured is the total capacitance of the stack. This corresponds to both insulator layers and the phosphor layer capacitances in series with each other. When the threshold voltage of the device is exceeded and luminescence occurs, the phosphor layer is essentially shorted and the remaining capacitance of the stack is simply both insulator capacitances in series. For the ZnS:Tb structure the insulator capacitance is approximately 2-4 nF while the total capacitance is around 0.6 nF. The C-V graph also provides information on the presence of space charge within the phosphor. A C-V curve for ZnS:Tb is shown in Fig.2-8. The overshoot on the C-V curve indicates the existence of space charge. Samples with less space charge will show only a slight overshoot. Space charge is generated by ionized donors in the phosphor, such as defects or impurities. This bulk charge causes the field across the phosphor to be nonuniform which results in the bending of the bands inside the phosphor. Because not much space charge is present in current ALE or sputtered samples, the effects of space charge are neglected in this work.

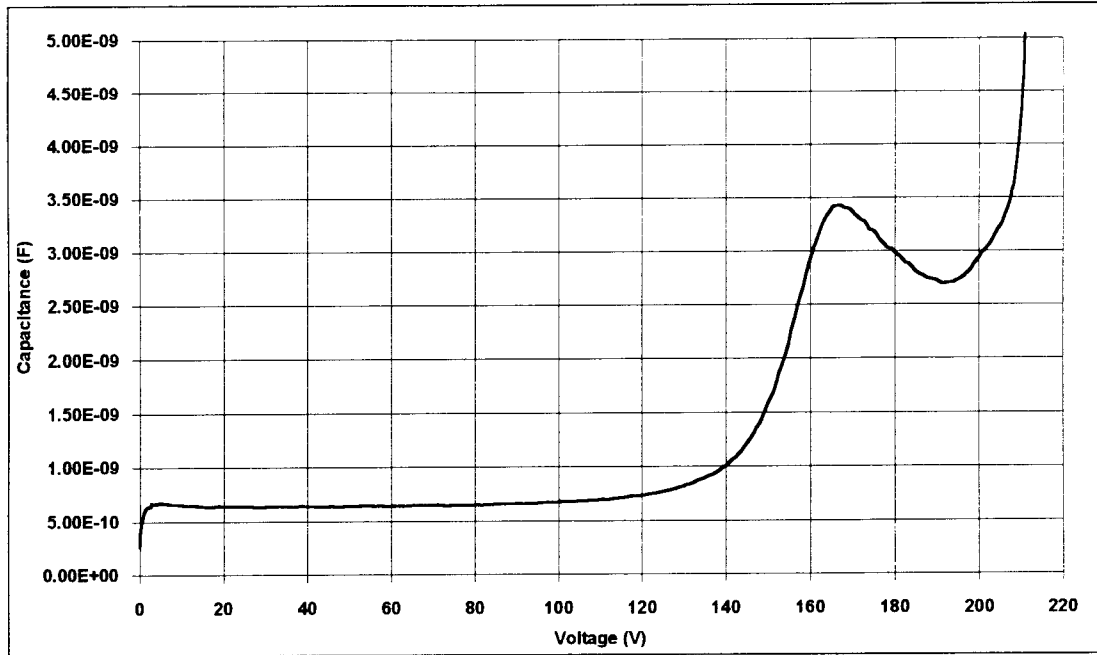


Figure 2-8. C-V curve for ZnS:Tb.

The Q-V [3,6,7] curve is generated by plotting the time integral of the current versus the externally applied voltage.

$$Q_{\text{ext}} = \int i(t) dt \quad (2-4)$$

From this method the polarization charge, the insulator and total capacitance, the turn-on voltage, and leakage charge between pulses can be determined. These parameters can easily be found by inspecting a Q-V graph. Figure 2-9 shows a typical Q-V curve. The internal charge is calculated using the following equation [20].

$$q(t) = \frac{C_i + C_p}{C_i} C_{st} V_{st}(t) - C_p (V_{ext}(t) - V_{st}(t)) \quad (2-5)$$

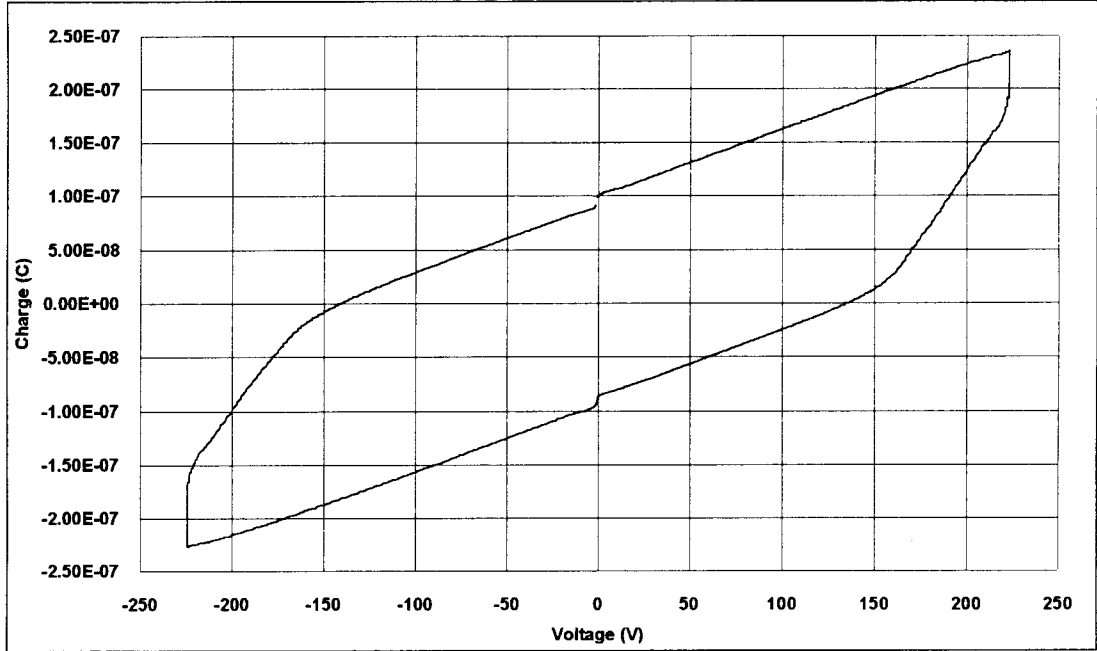


Figure 2-9. Q-V curve for ZnS:Tb.

Yet another useful way to obtain information about the electrical characteristics of TFEL devices is the $Q - F_p$ [6,7] technique. Here the charge within the phosphor Q_{int} is plotted with respect to the internal phosphor field F_p . Q_{relax} is the relaxation charge which flows across the phosphor during the portion of the waveform at which the applied voltage is constant at its maximum value. This relaxation charge causes the phosphor field to relax. The internal or polarization charge is

$$Q_{int}(t) = \frac{C_i + C_p}{C_i} Q_{ext(t)} - C_p V_{ext}(t), \quad (2-6)$$

and the internal phosphor electric field is given by

$$F_p(t) = -\frac{C_i V_{\text{ext}}(t) - Q_{\text{int}}(t)}{d_p(C_i + C_p)}. \quad (2-7)$$

By inserting Eqn. (2-6) into Eqn. (2-7), we find that

$$F_p(t) = -\frac{1}{d_p} \left(V_{\text{ext}}(t) - \frac{Q_{\text{ext}}(t)}{C_i} \right), \quad (2-8)$$

while the internal insulator electric field is given by

$$F_i(t) = -\frac{C_p V_{\text{ext}}(t) + Q_{\text{int}}(t)}{d_i(C_i + C_p)}. \quad (2-9)$$

By inserting Eqn. (2-6) into Eqn. (2-9), we get

$$F_i(t) = -\frac{1}{d_i C_i} Q_{\text{ext}}(t). \quad (2-10)$$

Both equations 2-8 and 2-10 for $F_p(t)$ and $F_i(t)$, respectively, can be rewritten in terms of external quantities which can easily be measured, provided that C_i and C_p are known. C_i and C_p can be found from the C-V measurement. Then the equations simplify to

$$F_p(t) = -\frac{1}{d_p} \left(\frac{C_{\text{st}}}{C_i} V_{\text{st}}(t) - V_{\text{ext}}(t) \right) \quad (2-11)$$

and

$$F_i(t) = -\frac{1}{d_i} \frac{C_{st}}{C_i} V_{st}(t) \quad (2-12)$$

where C_{st} is the sense element capacitance referred to as the Sawyer-Tower capacitance [1].

A typical $Q-F_p$ graph is shown in Fig. 2-10. This method is helpful in assessing the polarization charge, leakage charge, and field-clamping.

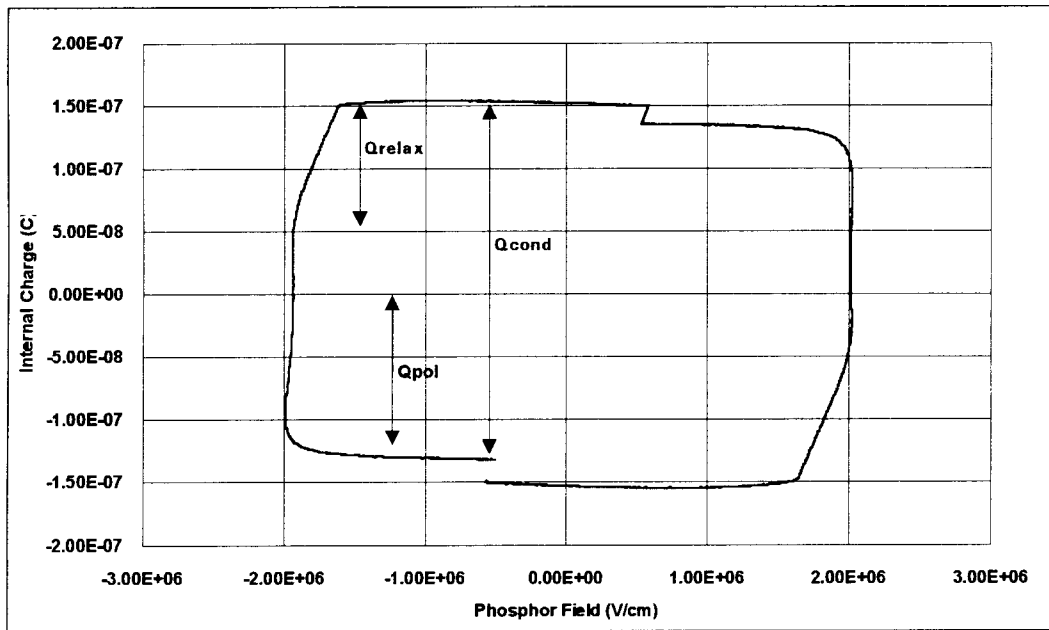


Figure 2-10. $Q-F_p$ curve for ZnS:Tb.

Figure 2-11 shows the experimental setup for measuring these external quantities.

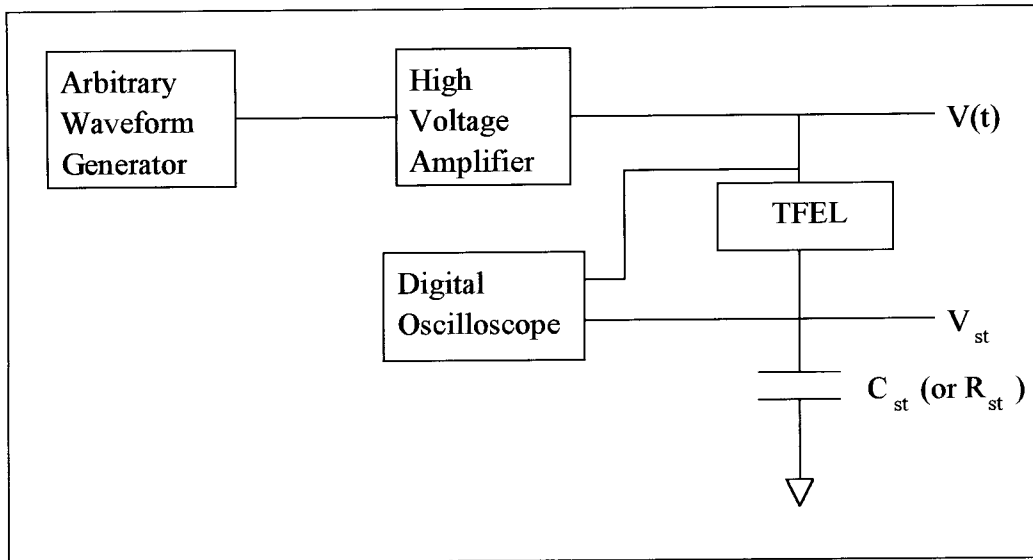


Figure 2-11. Experimental setup for electrical measurements.

2.5 Electron Transport

The electron energy distribution during conduction is still a topic of controversy. No exact verification of predicted electron energy distributions has yet been accomplished. Krupa [8] has performed measurements in 1971 and indicated that they could be used to probe the hot electron energy distribution.

Once the externally applied voltage reaches the threshold voltage of the device, electrons can tunnel from the insulator/phosphor interface states into the ZnS conduction band. If the electrons gain energies greater than 2.54 eV from the phosphor field, they can impact-excite the Tb luminescent centers which then de-excite and give off photons of characteristic wavelengths. At the moment not much is known about the actual hot electron energy distribution within the phosphor. In order to use accurate simulation

programs to predict the efficiency of different materials, it is important to find this distribution.

Several papers have been published on the simulation of these devices and the determination of the high energy tail of the electrons distribution. According to the calculations by Brennan [9], carriers in ZnS barely reach high enough energies to generate luminescence. This approach includes the full details of the first two conduction bands as well as the full-order treatment of the electron-phonon scattering mechanisms.

A nonparabolic multivalley band structure model simulated by Bhattacharyya et al. [10] and Pennathur [11] gives a distribution close to what is expected through experiment. Scattering mechanisms associated with optical and acoustic phonons, and impurities are included in this model. The steady-state electron distribution at high fields is shown to be sufficient enough to explain the observed efficiency of ACTFEL devices. The results also show that with increasing phosphor field an increasing number of electrons are energetic enough to produce ZnS band-to-band ionization, even though a significant amount of carriers are not heated above 5 eV.

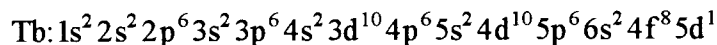
In contrast, the results obtained by Mueller et al. [12,13] state that the majority of carriers in the phosphor gain very high energies, thus producing band-to-band impact ionization. Average electron energies are believed to reach 6-9 eV.

Obviously, there is some controversy regarding the transport mechanism in ACTFEL devices. There is a need to generate experimental results which can shed some light on the transport mechanism.

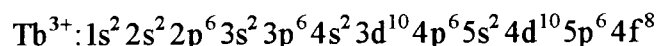
2.6 Tb³⁺ Energy Levels and ZnS Crystal Lattice Interaction

In order to accurately assess the perturbation of the terbium energy levels caused by the zinc sulfide crystal lattice interaction, one needs to know about the electronic

configuration of the valence electrons of the terbium ion. Terbium has the atomic number 65 and has the following electronic configuration:



The Tb^{3+} -ion contains three less electrons and has the configuration



The terbium atom has lost three electrons, two from the 6s and one from the 5d orbital. The eight valence electrons reside in 4f orbitals. The arrangement of these electrons determines the ground and excited states of Tb^{3+} . Each atomic state can be unambiguously determined by a set of four quantum numbers. For an electron, these quantum numbers are denoted by small letters, whereas for an atom, they are denoted by capital letters. One set of quantum numbers classifying an individual electron is $\{n, l, m_l, s\}$. The quantum number n corresponds to the energy eigenvalues of the electron. The quantum number l represents orbital angular momentum and can take on values from 0 to $n-1$. The quantum number m_l represents the projection of angular momentum along one axis in space and can take on values from $-l$ to l . The quantum number s corresponds to the "spin" angular momentum of an electron and can have values of $+1/2$ or $-1/2$. There is no classical analogy to spin angular momentum. For a given atom, no two electrons can have identical sets of quantum numbers.

We now wish to describe all the electrons in an atom or ion. One way to do this is to sum the contributions of all the individual electrons. The electrons in filled states do not contribute, so we only consider the valence electrons. For example, consider the terbium ion, Tb^{3+} . There are eight valence electrons to be placed in seven f-orbitals. In the ground state (lowest energy state), electrons will occupy as many orbitals as possible

with the same spin angular momentum. Only when there are no more empty orbitals, do electrons with opposite spin fill a given orbital. Thus, in the ground state:

$$m_l : 3 \quad 2 \quad 1 \quad 0 \quad -1 \quad -2 \quad -3$$

$$\uparrow\downarrow \quad \uparrow \quad \uparrow \quad \uparrow \quad \uparrow \quad \uparrow \quad \uparrow$$

where the arrows indicate the spin (parallel or anti-parallel) of the individual electron. It is important to note that, according to Hund's Rule, electrons will occupy as many orbitals as possible with unpaired (parallel) spin. When all orbitals are filled with a single electron, then the occupation of the orbitals continues with paired (anti-parallel) spin. In the case of the terbium ion, m_l can take on different values, depending on which orbital the electron with anti-parallel spin resides.

$$m_l = l, l-1, l-2, \dots, -l \quad \text{f-orbitals}$$

The total orbital angular momentum of the terbium ion can be found by summing the angular momentum of each electron.

$$L = \sum m_l = 3$$

Similarly, the total spin angular momentum can be found by summing the spin of each electron:

$$S_{\text{Tb}^{3+}} = \sum m_s = 6 \left(\frac{1}{2} \right) = 3$$

We now introduce the total angular momentum of Tb^{3+} , as $J_{\text{Tb}^{3+}}$, the vector sum of the orbital and the spin angular momentum. This can take on values 6, 5, 4, 3, 2, 1, 0 (from $L+S$ to $L-S$). Two examples of the total angular momentum are shown in Fig. 2-12.

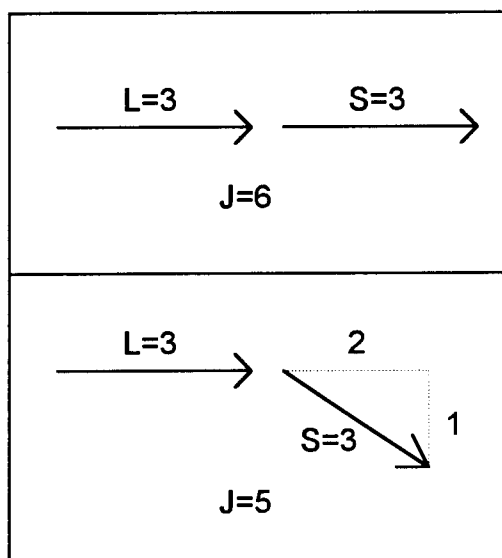


Figure 2-12. Examples of possible total angular momentum for the ground state of Tb^{3+}

In fact, the magnetic fields generated by the spin angular momentum interact with the orbital angular momentum. This "spin-orbit coupling" affects the total energy of the Tb^{3+} ion and splits the ground state energy into levels of J . Thus, to completely specify the energy of an electronic configuration of Tb^{3+} we need to account for the ion's orbital angular momentum L , the spin angular momentum S , and the total angular momentum J . Hence we label each state of the ion according to term symbols as follows:

$$^{2S+1}L_J$$

where

$$\begin{array}{rcccccl}
 \text{orbital} & \text{angular} & \text{momentum} & = & 0 & 1 & 2 & 3 \dots \\
 & & L & = & S & P & D & F \dots
 \end{array}$$

Hence, the ground state of Tb^{3+} is labeled 7F with the following multiplet "fine structure" $^7F_6, ^7F_5, ^7F_4, ^7F_3, ^7F_2, ^7F_1, ^7F_0$, each with slightly different energies. This splitting is illustrated in the energy level diagram shown in Fig. 2-13 below.

The first excited state for the terbium ion is formed when an electron "flips" as follows:

$$\begin{array}{ccccccc}
 m_l : & 3 & 2 & 1 & 0 & -1 & -2 & -3 \\
 & \uparrow\downarrow & \uparrow & \uparrow & \uparrow & \uparrow & & \uparrow\downarrow
 \end{array}$$

In this case, $L_{\text{Tb}^{3+}} = 2$ and $S_{\text{Tb}^{3+}} = 2$, so the proper term symbol is 5D . These levels also split according to J . The lowest two excited state energy levels are $J=4$ and $J=3$ which lie 2.54 eV and 3.25 eV above the ground state, respectively, as Fig. 2-13 illustrates [14]. For a more detailed discussion please refer to Herzberg [15].

There are many levels above 5D_3 but atoms excited into these levels decay very rapidly [16] and nonradiatively to the second luminescent level. There also exists a transition from 5D_3 to 5D_4 , but this transition occurs at a wavelength of approximately $1.77\mu\text{m}$ [17], and may be mostly nonradiative.

Once the terbium atom is inserted into the ZnS lattice, each energy level is perturbed. The amount of the perturbation of the terbium ion energy levels depends on the extent of the interaction of the outer electrons of the terbium with the ZnS host lattice. The interactions of an ion with a host lattice can be expressed by a Hamiltonian operator. The Hamiltonian of an ion in a crystal can be written as $H = H_F + H_{CF}$, where H_F is determined by the interaction within an atom of electrons with the nucleus, electrons with other electrons, and the spin-orbit interaction. H_{CF} represents the interaction between the

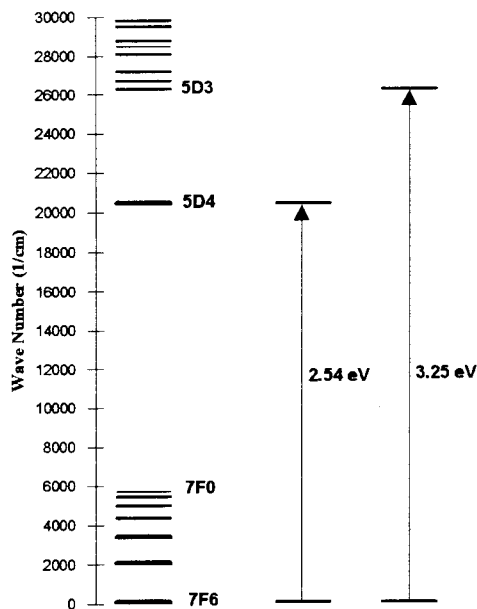


Figure 2-13. Energy level diagram of Tb³⁺.

ion and the host lattice. Depending in which shell the outer electrons of an atom lie, the crystal lattice interaction can vary significantly. In the case of 4d or 5d electrons, the crystal lattice interaction can broaden an energy level by as much as 40000cm^{-1} .

The interaction between the 4f electrons of the terbium ion and the crystal field of zinc sulfide is very weak. According to A. S. Marfunin [18], the crystal field splitting is of the order of $50\text{-}400\text{cm}^{-1}$ which broadens out each transition but does not severely affect it. Due to the fact that there is a very weak interaction between the host lattice and the terbium ion, each luminous transition, if strong enough, can be easily recognized in the spectrum of terbium. Table 2-1 shows the anticipated spectral peaks of the terbium ion both with and without the crystal field splitting. A maximum crystal field broadening of 400cm^{-1} is assumed. The fact that each transition is given as a range of wavelengths comes from the fact that, without the crystal lattice interaction, each luminescent level, as well as the ground level, contain multiplet levels. All multiplet levels have been combined

into a range of wave numbers; therefore, a range of wavelength is obtained when a transition from an excited level to a ground multiplet is shown. The wave number is

Transition	Wavelength Range	Wavelength Range
	No Crystal Field Splitting	Crystal Field Splitting included
	(nm)	(nm)
$^5D_4 - ^7F_6$	487.9-491.5	478.6-501.4
$^5D_4 - ^7F_5$	541.9-547.6	530.4-559.9
$^5D_4 - ^7F_4$	580.4-587.4	567.2-601.5
$^5D_4 - ^7F_3$	618.4-621.8	603.5-637.7
$^5D_4 - ^7F_2$	644.2-648.3	628.0-665.6
$^5D_4 - ^7F_1$	664.2-667.8	647.0-686.1
$^5D_4 - ^7F_0$	675.9-677.4	658.1-696.3
$^5D_3 - ^7F_6$	380.7-382.4	375.0-388.3
$^5D_3 - ^7F_5$	412.8-415.5	406.1-422.5
$^5D_3 - ^7F_4$	434.7-438.0	427.3-445.8
$^5D_3 - ^7F_3$	455.7-456.9	447.5-465.4
$^5D_3 - ^7F_2$	469.6-471.0	460.9-480.0
$^5D_3 - ^7F_1$	480.1-481.2	471.1-490.6
$^5D_3 - ^7F_0$	486.1-486.2	476.9-495.9

Table 2-1. Transitions of Tb^{3+} with and without crystal field splitting.

simply another representation of the wavelength where $w.n. = \frac{1}{\lambda(\text{cm})}$. The conversion

from wavelength to energy is as follows: $E(\text{eV}) = \frac{1.24}{\lambda(\mu\text{m})}$.

A full spectrum of terbium from an ACTFEL ZnS:Tb device, taken at a maximum applied voltage of 200 V, is shown in Figs. 2-14a and 2-14b. The spectrum ranging from 360 nm to 475 nm corresponds to the luminescence which originates from the 5D_3 level and ends in the ground manifold. The spectrum ranging from 475 nm to 675 nm corresponds to the luminescence which originates from the 5D_4 level and ends in the ground manifold. The light intensity originating from the 5D_4 level is much stronger than the light seen from the 5D_3 level, as shown by a 100x increase in sensitivity for Fig. 2-14a. At a wavelength of 543 nm a green-yellowish peak is found, the color which is characteristic for the Tb ion.

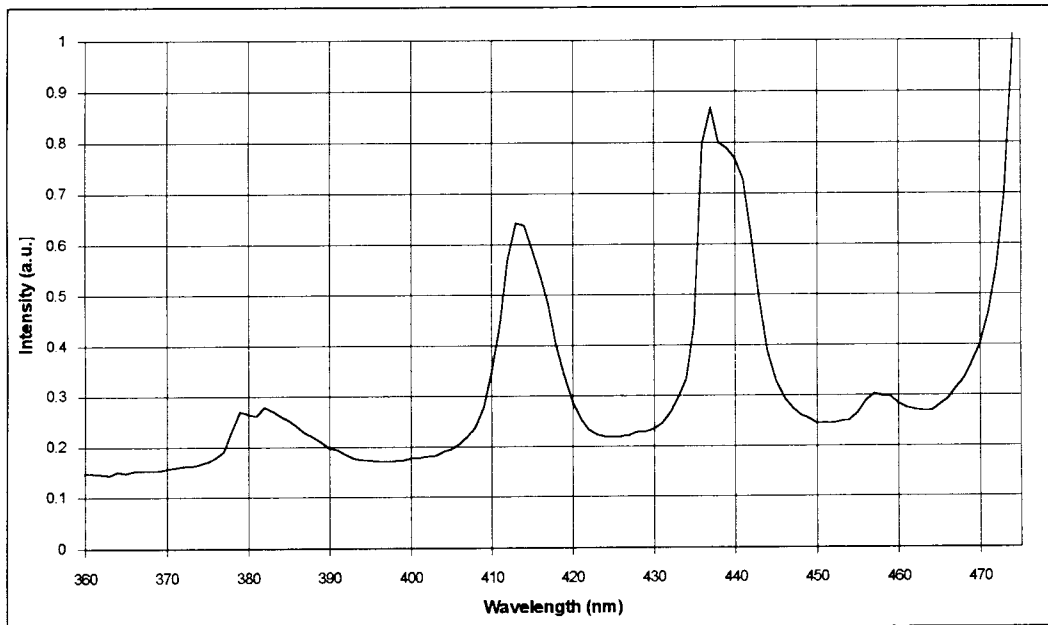


Figure 2-14a. Optical spectrum of ZnS:Tb from 360nm to 475nm.
Vertical scale is 100x expanded from Fig. 2-14b.

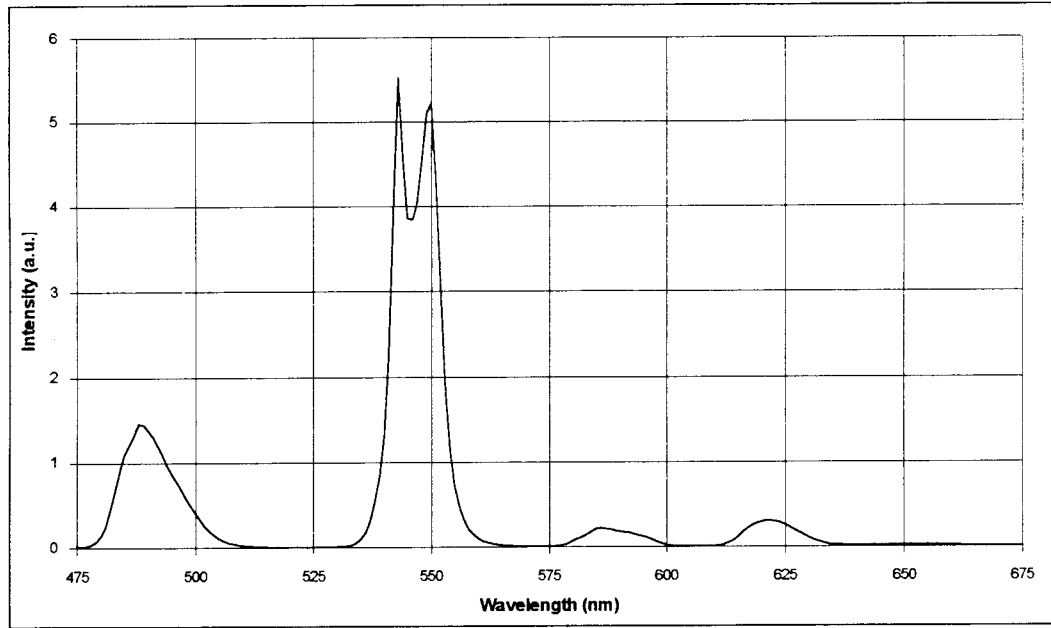


Figure 2-14b. Optical spectrum of ZnS:Tb from 475nm to 675nm.

The Tb spectrum is in agreement with the optical experiments conducted Thomas et al. [19], showing that the transitions from the 5D_4 level to the ground manifold extend from 470nm to 700nm, and that transitions from the 5D_3 level extend from 360nm to 480nm.

In order to avoid confusion throughout the report, the 5D_3 level is referred to as the upper luminescent level and the 5D_4 level as the lower luminescent level.

2.7 Review of Experiments Conducted on ZnS:Tb

Research on the luminescence of rare earth materials, especially of terbium, extends back into the 1970s. Krupka [8,20], Tanaka [21], and Mikami [22] investigated

the luminescence of ZnS:TbOF evaporated samples, determined that the brightness of the device is a function of the concentration of the luminescent impurity, and found that impact excitation is the dominant excitation mechanism. A detailed theoretical analysis on ZnS luminescence is given by Bringuier [23]. More recently, hot electron luminescence has been investigated in ZnS:Mn samples by Douglas et al. [24].

Krupka [8] conducted experiments at 77 K in which the ratios of the intensities of the $^5D_3-^7F_4$ transition to the $^5D_4-^7F_6$ transition are plotted versus the maximum applied voltage. Initially, this ratio provides information on the behavior of the luminescence with changing Tb concentration. Krupka came to the conclusion that this ratio of intensities also provides a measure of how many Tb ions are excited beyond an energy of 3.25 eV, which in turn reflects how many carriers inside the phosphor have energies exceeding 3.25 eV. Results show that the ratio of intensities increases and reaches saturation at large applied voltages. This indicates a heating of the electron distribution with increasing applied voltage. The driving voltages used by Krupka are both sinusoidal and square pulsed waveforms.

This approach initially served as the basis for the experiments which follow. However, after further research it is determined that the ratio of intensities, measured as by Krupka, does not provide an accurate indication of the extent of the carrier heating with increasing voltage. Reasons for this conclusion are that nonradiative transitions between luminescent energy levels are not considered and that the applied square and sinusoidal waveforms do not create a constant field in the phosphor. In order to determine the exact hot electron energy distribution, all carriers must be subjected to the same conditions. The field must be held at a constant value. Also, the existence of nonradiative transitions between two excited levels or between excited levels and the ground level are not accounted for when simply using the ratio of intensities of the $^5D_3-^7F_4$ and $^5D_4-^7F_6$ transitions. More detail on these issues is given in the following chapters.

3.0 Experimental Setup for Luminescence Measurements

3.1 Introduction

In order to understand the device physics of these devices, it is necessary to measure them at room temperature as well as low temperatures. Both the standard voltage waveform used in EL devices as well as a field-controlling waveform are used in this report. In the standard waveform pulses, the electric field changes during the applied voltage pulse due to electrons moving internally from one insulator/phosphor interface to the other. The field-control waveform holds the electric field constant inside the phosphor material through a feedback circuit and ensures that the same field condition exists within the sample for all electrons contributing to the conduction current.

By determining the areas under the time-resolved spectra peaks for the given wavelength ranges, it is possible to take the ratio of these areas and obtain a measure of the percentage of terbium atoms excited into the 5D_3 level. By taking time-resolved spectra for various electric fields, it is possible to plot the intensity ratio (or area ratio) versus the internal phosphor electric field.

Through experiment it has been determined that taking the ratios of the peak areas yields the same trend as taking the ratios of simple peak amplitudes (a much quicker measurement). For this reason it was decided to use the peak ratios by selecting one peak in the upper level transitions, at 437nm, and by selecting two lower level transition peaks, at 489nm and 543nm.

According to Krupka [9], the ratio of the 437 nm peak to the 489 nm peak determines the relative percentage of electrons which are energetic enough to excite terbium ions into the 3.25eV upper luminescent level.

In contrast to Krupka's experiments, the tests conducted in this work employ two types of waveforms. One is a trapezoidal waveform with 5 μ s rise and fall times and a 30 μ s peak voltage (Fig. 3-1). Each pulse is followed by one with opposite polarity. This waveform is currently used in all commercial EL devices. The only difference is that for these experiments the waveform is at a frequency of 100 Hz, while the normal commercial operation frequency is at 60 Hz or 10 kHz. The reason for the low frequency here is that the luminescence resulting from each voltage pulse has a decay time of several milliseconds. The low frequency ensures that sufficient time is given for the luminescence to decay completely before the next voltage pulse is applied.

The other waveform, shown in Fig. 3-2, uses a field-control circuit to stabilize the internal phosphor field of the ACTFEL device. This provides a better condition for finding the hot electron distribution because all carriers are subject to the same electric field. This field-control circuit was first introduced by Douglas [6]. Douglas uses a 100 Hz waveform where every tenth pulse is replaced with a field-control pulse. The waveform used in this work increases the repetition rate of the field-control pulse from 10 Hz to 50Hz. The higher repetition rate provides a higher averaging rate and, consequently, a better signal-to-noise ratio. A succession of high frequency and high voltage pulses is inserted between field-control pulses so that a steady state can be established in less time and the field-control pulse can be applied at a higher frequency. Also, the voltage of these high frequency pulses determines the lowest phosphor field necessary to obtain luminescence. The reason for this is that with these high frequency pulses, the magnitude of the voltage determines the amount of polarization charge present at the start of the field-control pulse. This is only true for small phosphor fields. At larger fields the field-control pulse is able to extract more charge from interface states than the high frequency pulses can provide. Then the polarization charge is determined by the length and height of the field-control pulse.

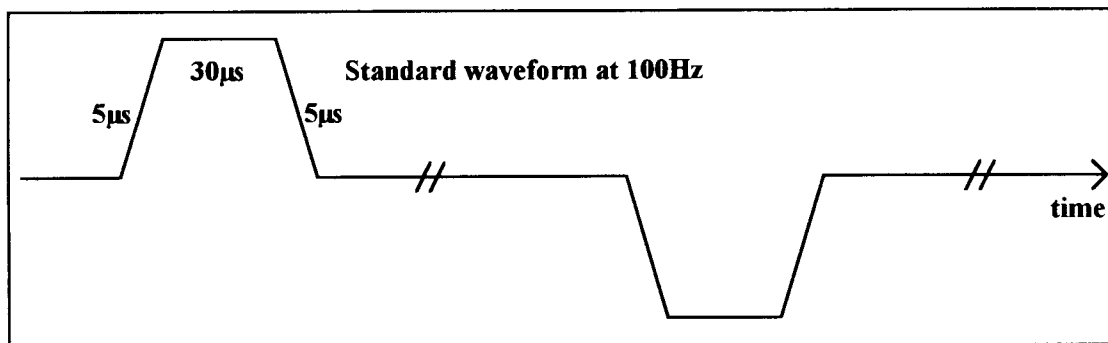


Figure 3-1. Standard Voltage Waveform.

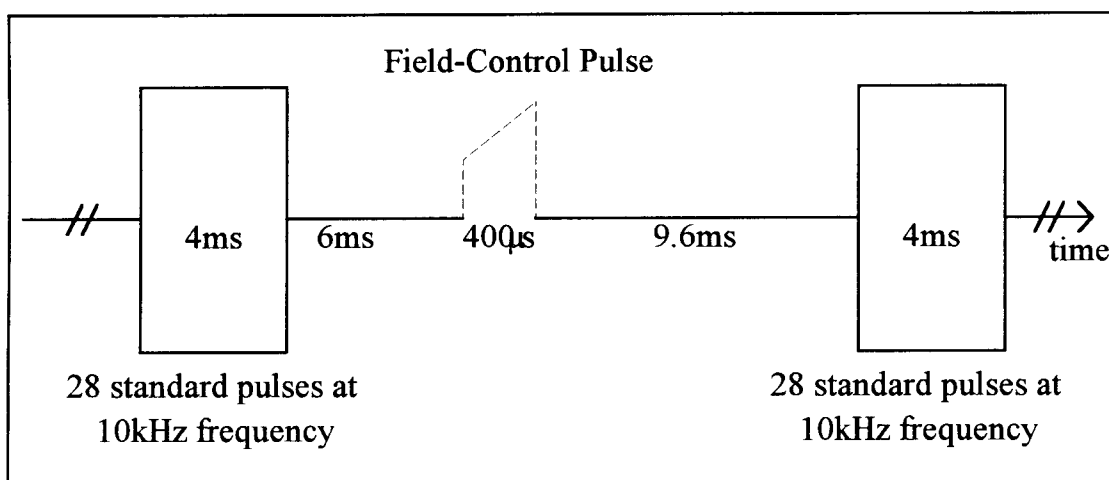


Figure 3-2. Driving waveform including the field-control pulse.

3.2 Experimental Setup

During a regular trapezoidal voltage pulse, as shown in Fig. 3-1, the field is not constant. The field-control circuit, which uses a feedback loop, ensures that the electric field inside the phosphor is maintained for a given period of time, i.e. long enough to obtain accurate spectral data. The height of the field-control pulse is set to give the

desired electric field. Then the luminescence at specific wavelengths is measured. At each wavelength a luminescence pulse occurs with a characteristic height and decay time. The maximum value of each pulse is used as the representation of the pulse.

In order to keep the electric field constant within the phosphor, the applied voltage to the sample needs to change during each pulse. As the pulse is applied, a certain electric field exists within the phosphor. But during the pulse electrons are extracted from interface states and are accelerated toward the other side of the material. There the electrons are captured by interface states. There is a buildup of negative charge at this interface which generates an electric field opposing the one created by the voltage pulse. In effect, the electric field that is present in the phosphor is lowered. In order to keep this field at a constant value, the applied voltage must compensate for this buildup of charge and subsequent generation of an opposing field. The applied voltage needs to be increased. This is the reason why the field-control voltage pulse has a rising slope.

From the charge on the Sawyer-Tower sense capacitor, the phosphor field is given by

$$F_p = -\frac{1}{d_p} \left(\frac{Q_{st}}{C_i} - V_{ext} \right) \quad (3-1)$$

where d_p is the phosphor thickness, C_i is the insulator capacitance, $Q_{st} = C_{st} V_{st}$ is the external charge where C_{st} is the sense capacitance, V_{st} is the voltage across the sense capacitor, and V_{ext} is the externally applied voltage..

In order to keep the field constant, the external voltage, V_{ext} , needs to vary according to

$$V_{ext} = -\frac{C_{st}}{C_i} \left(V_{st} - \frac{C_i}{C_{st}} d_p F_p \right). \quad (3-2)$$

A field-control circuit is used to generate the constant phosphor field. The experimental setup is shown in Fig. 3-3.

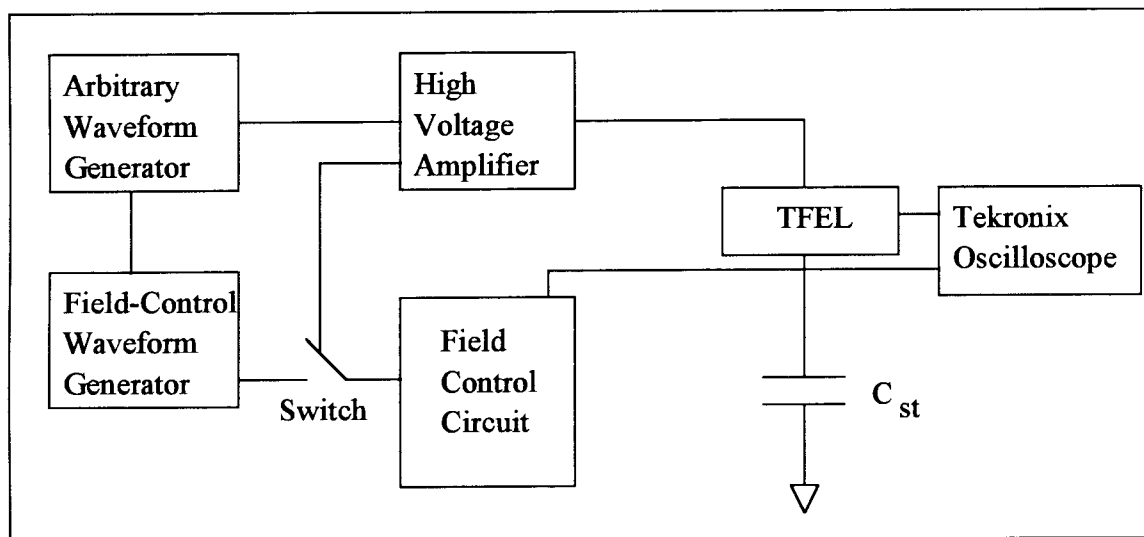


Figure 3-3. Field-control experimental setup.

This experimental setup periodically generates a constant field during part of the driving waveform. The arbitrary waveform generator creates the waveform which drives the TFEL device. The frequency of this generator is 50 Hz. The high voltage amplifier amplifies the signal to drive the device. During one portion of the period, a 10kHz signal of the standard waveform (5 μ s rise time, 30 μ s peak, 5 μ s fall time) drives the device at a voltage much larger than the threshold voltage. This high frequency and applied voltage ensures that most of the interface states are filled up with electrons. During the second portion of the waveform period, the field-control pulse is applied. The time gap between the high frequency pulses and the field-control pulse is to ensure that the luminance caused by the high frequency pulses has completely decayed before the field-control pulse is initiated. The duration of the constant field is approximately 400 μ s. The field control pulse is not part of the regular waveform but is generated by the field-control circuit and

inserted into the waveform via a switch. Figure 3-4 shows the field-control circuit. Fig. 3-2 shows the field-control waveform with the field-control pulse.

3.2.1 Diagram of the Field-Control Circuit

The field-control must maintain a steady electric field in the phosphor layer for the duration of the field-control pulse. If there is any change in voltage across the device the voltage across the sense element will reflect that. The feedback loop detects any change in voltage across the sense element and modifies the input voltage to the high voltage amplifier so that the phosphor field inside the device is maintained. Figure 3-4 shows the layout of the field-control circuit.

In order to obtain a graph of the ratio of luminescence transitions versus the internal phosphor field, a range of desired electric fields must be chosen, between 0.5 MV/cm and 2.2 MV/cm. For each electric field the corresponding voltage V_{ext} is calculated according to Eqn. 3-2. The phosphor thickness d_p as well as the insulator and sense capacitances need to be known. If the insulator capacitance is not known, a C-V or Q-F_p measurement, as explained in Chapter 2.4, will provide that value. Once all parameters are known, V_{ext} can be calculated. Next the field-control pulse height is adjusted to V_{ext} . The spectral measurement can now be obtained.

One possible approach is to take a full spectrum of the luminescence. Two spectra need to be taken for every given electric field. The first spectrum is taken from 360 nm to 475 nm. This range covers the transition of the second luminescent level to the ground manifold. The intensity here is very low and the PMT supply voltage is set to -1000 V, giving a signal amplification of 10^7 . The second spectrum is taken from 475 nm to 675 nm. This range covers the transition from the first luminescent level to the ground manifold. This spectrum is much higher in intensity and contains the

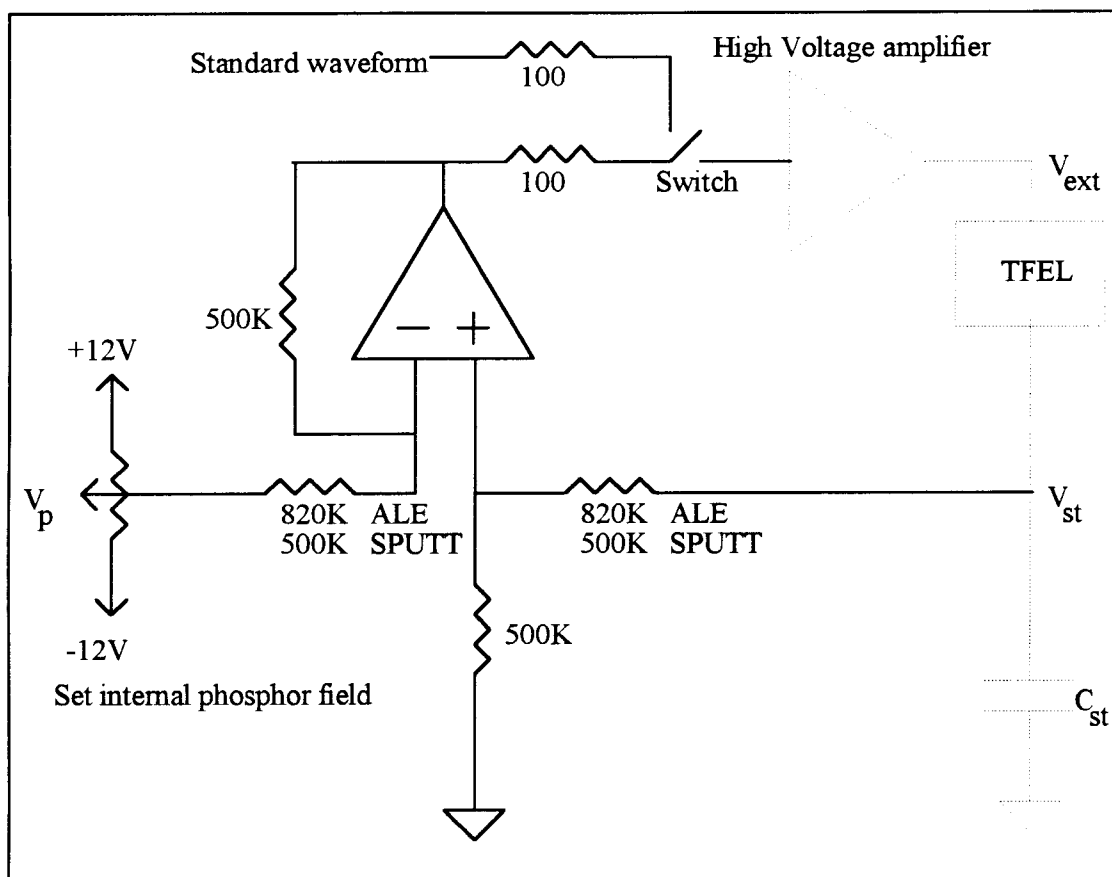


Figure 3-4. Diagram of the field-control circuit.

characteristic green luminescence for which the terbium-doped zinc sulfide phosphor is known. The PMT supply voltage is set to -500 V, giving a signal amplification of 10^5 . Once the time-resolved spectra are taken, the field-control pulse is set to a new voltage, corresponding to a new field, and the spectra are retaken. Once a set of spectra at different fields is taken, the next step is to calculate the area under the 360 nm to 475 nm and 475 nm to 700 nm spectra. Background noise needs to be eliminated. Also, the amplification of the PMT needs to be accounted for. The ratio of areas is then plotted versus the phosphor field to give the desired graph.

Initially, this approach was used. Because this approach is very time consuming, a simpler approach was used.

The simpler approach is to pick two distinct peaks from each transition and record them as a function of the phosphor field. The ratio of these two values versus the applied field gives an indication of the how the electrons are distributed. Experiments have shown that both methods yield the same trends in the ratio, they only differ by a constant. Therefore the latter method was chosen.

3.2.2 Optical Setup and Measurement Techniques

The main focus of this work is to use spectral measurement techniques to obtain information on the energy distribution of electrons within the phosphor.

The sample is placed in a holder and fastened onto the cold stage of a closed-cycle helium refrigeration system. This system is capable of being pumped to low pressure levels or to be backfilled with dry nitrogen. The phosphor is hygroscopic and water vapor needs to be kept away so that the sample does not deteriorate in performance. This system is also capable of being cooled to very low temperatures, another feature which is important in the later stages of this work.

Two lenses collimate and focus the light from the sample onto the entrance slit of a Chromex 500SM 1/2 Meter Monochromator. A Hamamatsu R928 photomultiplier tube amplifies the signal. It is then fed into a Tektronix 420 digital oscilloscope where the signal waveform is averaged for smoothing purposes, and then downloaded onto a 486DX/66 PC. The layout of the system is shown in Figure 3-5. Communication between the computer and the oscilloscope is done via the GPIB (General Purpose Interface Bus) connection. The monochromator is controlled by LabWindows software. Data is taken from the oscilloscope using the same software.

The output of the PMT is in the form of a current. The input resistance of the oscilloscope is set to $1\text{ M}\Omega$. The voltage seen on the oscilloscope is therefore the product of the current and the $1\text{ M}\Omega$ resistance.

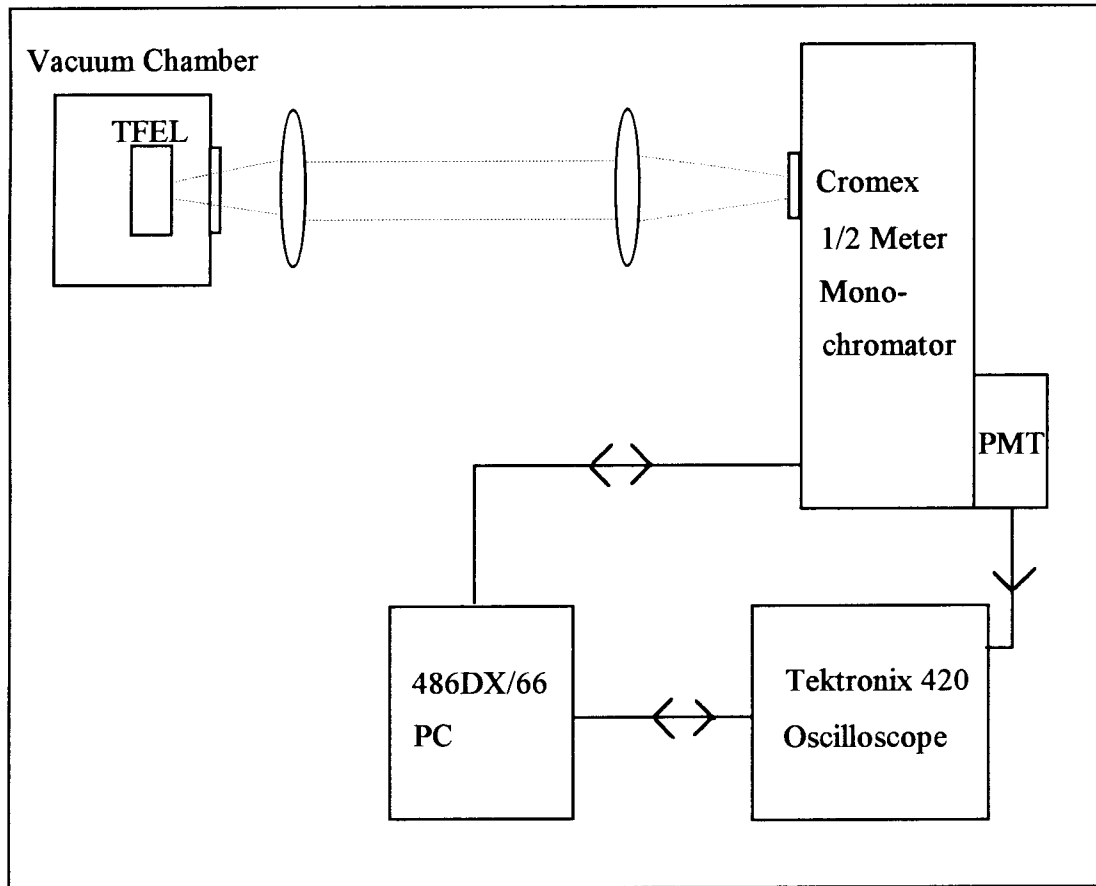


Figure 3-5. Optical setup

The PMT uses a dynode configuration to amplify the incoming photons. As a photon impacts on the cathode of the PMT, electrons are ejected from it (photo emission). These electrons are accelerated towards the first dynode which is at a higher potential. Electrons striking this dynode are multiplied and accelerated toward the next dynode. After a number of dynodes, many electrons impact onto the anode and produce a current.

The amount of amplification due to this dynode configuration depends on the voltage applied across the PMT. The PMT supply voltage generally varies between -200 V and -1000 V. For very weak signals a large negative voltage is applied to obtain the necessary amplification.

Table 3-1 shows some of the PMT supply voltages and the corresponding amplification factors.

Voltage (V)	Current amplification
-400	2.00E+04
-500	1.00E+05
-700	1.00E+06
-1000	1.00E+07

Table 3-1. Current amplification of the 928 Hamamatsu PMT

4.0 Hot Electron Luminescence

4.1 Introduction

In this chapter samples fabricated by both the ALE and the sputtered deposition method are investigated. In the first section data obtained by applying the standard voltage waveform is shown. The second section deals with measurements taken while the field-control waveform is applied. Room and low temperature measurements are taken.

As the voltage is increased the interface states fill up with more and more with electrons, thus making an increasing number of electrons available for conduction. This means that as the voltage is increased, a number of electrons are available to excite terbium ions into upper energy levels.

There exists the possibility of a radiative or a nonradiative transition between the first two excited levels (5D_3 – 5D_4). The energy difference between these levels corresponds to the energy difference between the lowest and highest energy level in the ground manifold. It is therefore quite possible that most of this transition is a multi-phonon transition and, therefore, nonradiative. The energy difference of 0.7 eV translates into a wavelength of 1.7 μm . A germanium detector was used to determine any luminescence at that wavelength but nothing was found. At low temperature this transition should vanish because it is a transition dependent on the interaction with phonons and is therefore dependent on the lattice motion.

Other possible nonradiative transitions exist from excited levels directly to the ground manifold. The radiative transitions seen in the optical spectrum of Tb^{3+} might be only a small percentage of the total transition rate from this level. Nonradiative transition could possibly dominate each transition. For this reason it has been concluded that the approach used by Krupka [9] to determine the hot electron distribution, is not a valid

approach because it does not take into account the nonradiative transitions. The ratio of the intensities, in which the intensity from the 5D_3 level is divided by the intensity from the 5D_4 level, does not reflect the percentage of hot electrons with energies above 3.25 eV.

The second part of this chapter focuses on experiments using a field-control voltage waveform. The luminescence during this field-control pulse is observed and evaluated. The field-control pulse ensures that the field is held constant. The high frequency pulses preceding the field-control pulse (see Fig. 3-2) ensure that a steady state is achieved.

4.2 Standard Voltage Waveform Experiments

4.2.1 Room and Low Temperature Experimental Results

Figure 4-1 shows the luminescence of ZnS:Tb as a trapezoidal voltage pulse is applied. The wavelength is 543nm which corresponds to the largest peak in the terbium spectrum, a green-yellowish color.

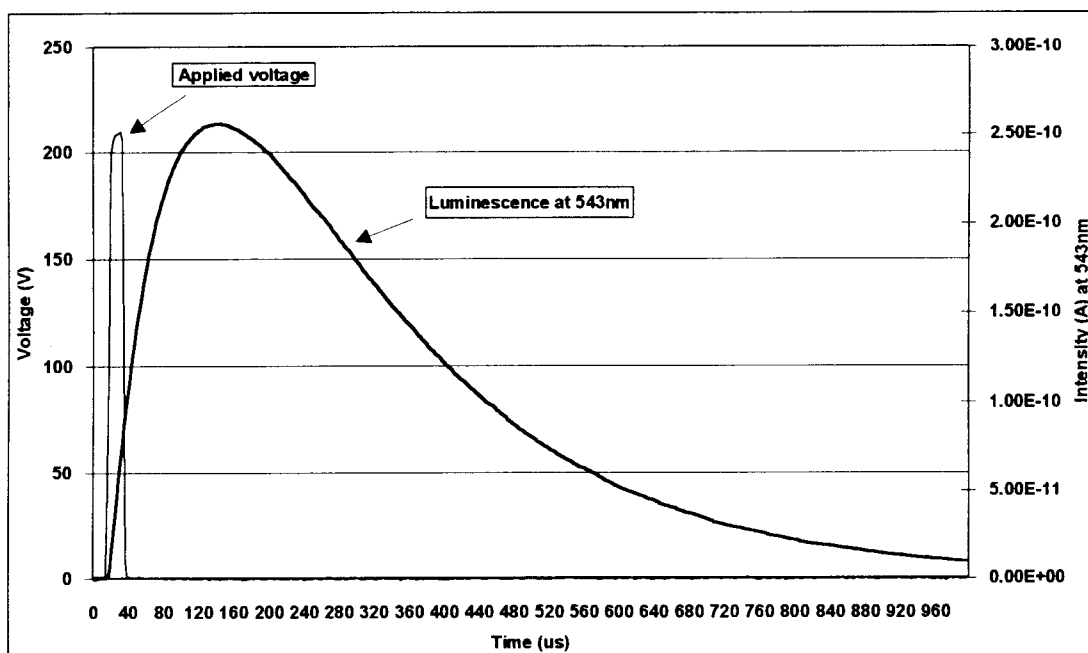


Figure 4-1. Trapezoidal voltage pulse and luminescence at 543 nm.

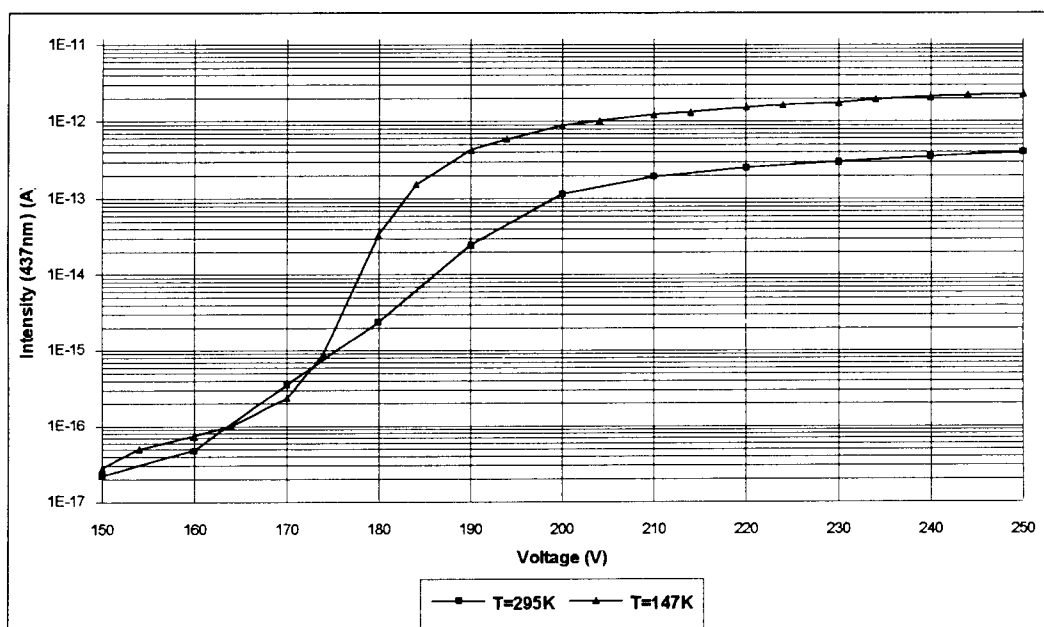


Figure 4-2. Intensity at 437 nm at T=295 K and T=147 K for the ALE sample.

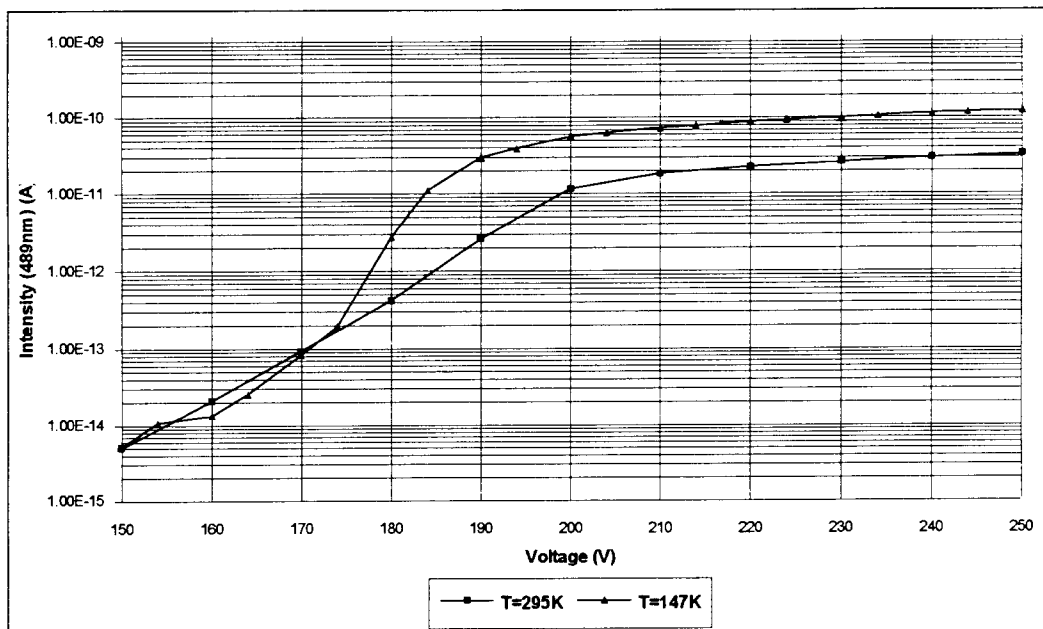


Figure 4-3. Intensity at 489 nm at $T=295\text{ K}$ and $T=147\text{ K}$ for the ALE sample.

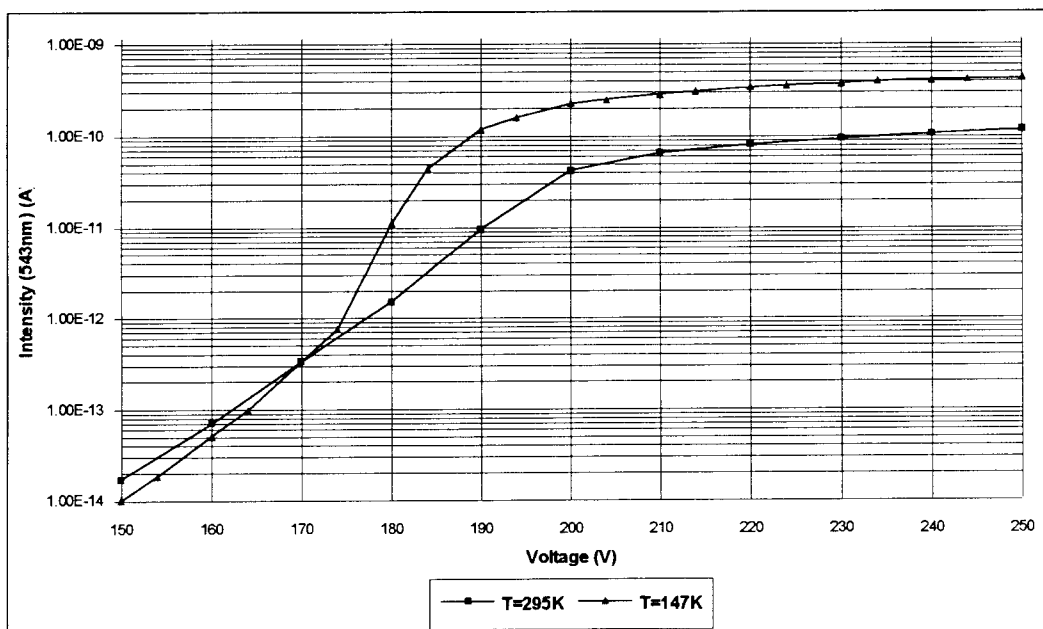


Figure 4-4. Intensity at 543 nm at $T=295\text{ K}$ and $T=147\text{ K}$ for the ALE sample.

By inspection of Figs. 4-2, 4-3, and 4-4, it can be seen that the intensity of all wavelengths saturates around 200V. Also, the 543nm peak is about three times larger than the 489 nm peak. The 437 nm peak is very much weaker than the others because it is part of the 5D_4 energy level and lies at 3.25 eV.

The onset of the rapid increase in luminescence for 437 nm is seen to occur at approximately 160-170 V for both temperatures. At low temperature luminescence increases drastically for all wavelengths, as is seen in Figs. 4-2, 4-3, and 4-4. Possible reasons for this increase are reduced scattering rates due to reduced lattice vibrations, and a change in nonradiative transition rates due to the reduction of optical phonons. More detail is given in the discussion.

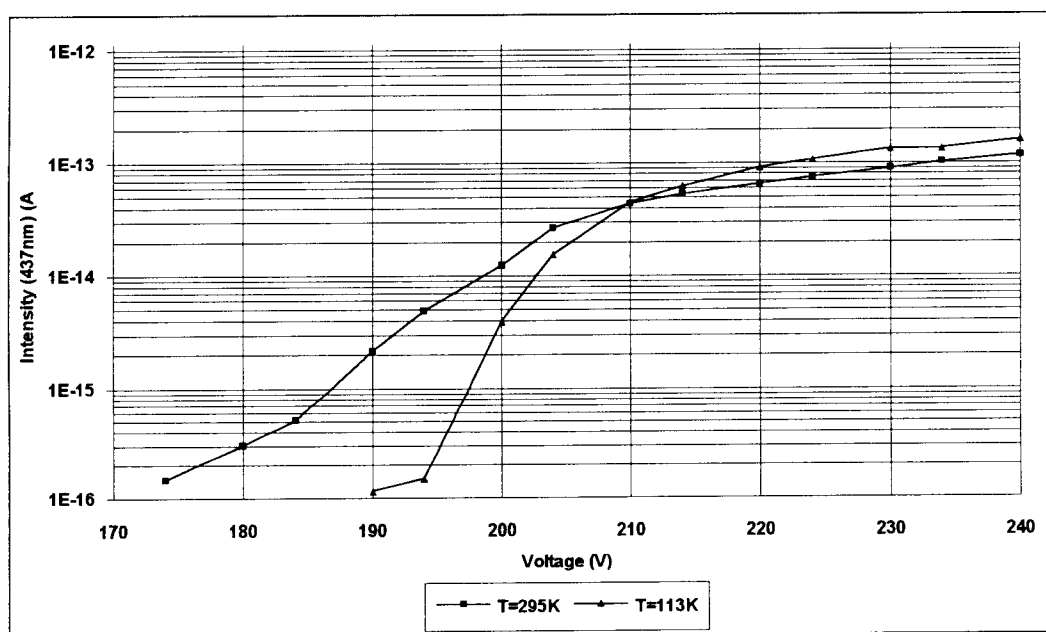


Figure 4-5. Intensity at 437 nm at T=295 K and T=113 K for the sputtered sample.

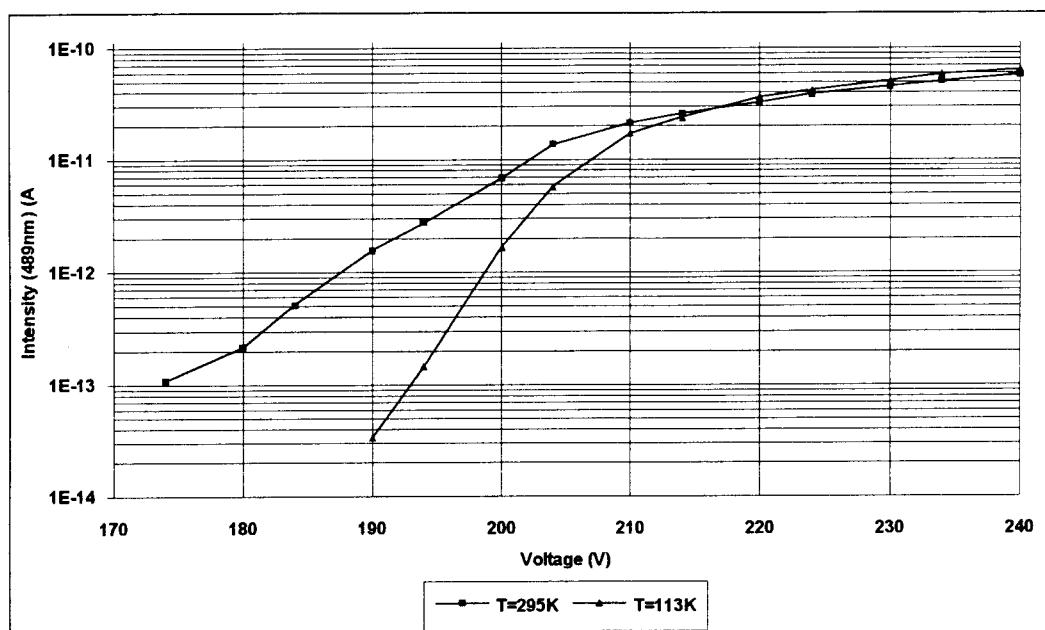


Figure 4-6. Intensity at 489 nm at T=295K and T=113K for the sputtered sample.

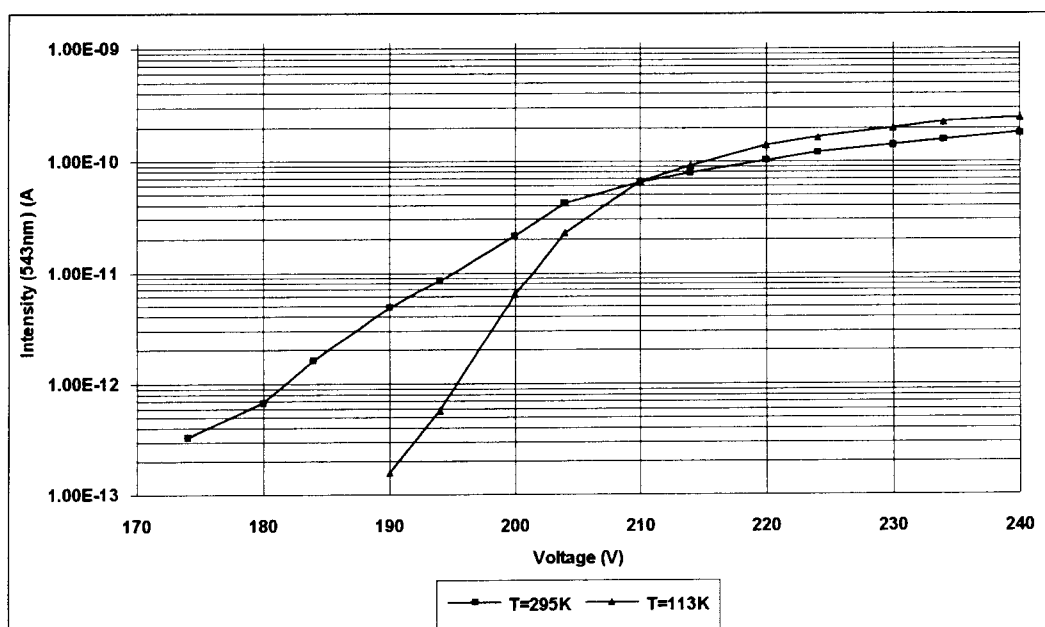


Figure 4-7. Intensity at 543nm at T=295K and T=113K for the sputtered sample.

Sputtered samples exhibit a different trend in luminescence when the temperature of the sample is lowered. Figures 4-5, 4-6, and 4-7 show a much lower increase in luminescence at lower temperature. These results can be attributed to a change in scattering and a change in nonradiative transition rates at low temperature.

The ratio of the intensity at a wavelength 437 nm and 489 nm is shown in Fig. 4-8 and 4-9 for the ALE and the sputtered sample, respectively. The ALE sample exhibits an increase and saturation in this ratio. This is consistent with the results obtained by Krupka [9]. The ratio indicates a heating of the electron energy distribution at higher voltages, for both low and room temperature. However, a quantitative answer to the electron distribution cannot be made because possible nonradiative transitions change the actual amount of electrons which do reach energies large enough to excite luminescent centers into the 5D_3 level (3.25 eV). If nonradiative transitions were minimized, the ratio would give a percentage of electrons above energies of 3.25 eV. But here the low temperature reached is 147 K, and it is not low enough to completely stop nonradiative transitions. Experiments conducted by Krupka were performed at 77 K. At this temperature the nonradiative transitions are lower than at 147 K.

The ratio for the sputtered sample show the same trend as the ALE sample, although the increase in ratio is less and saturation is reached much faster.

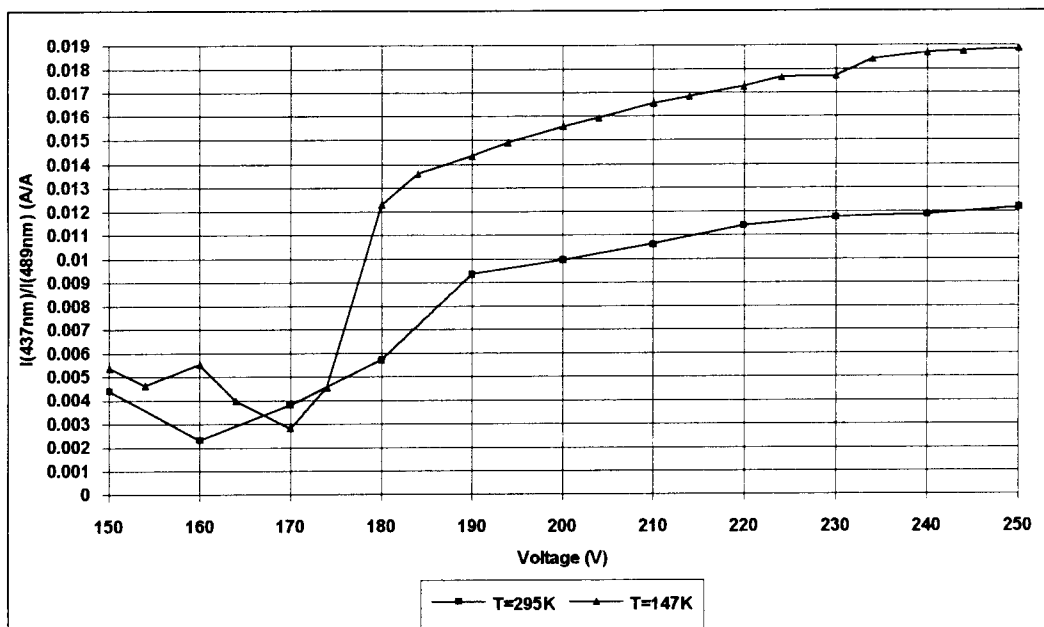


Figure 4-8. Ratio $I(437\text{nm})/I(489\text{nm})$ at $T=295\text{K}$ and $T=147\text{K}$ for the ALE sample.

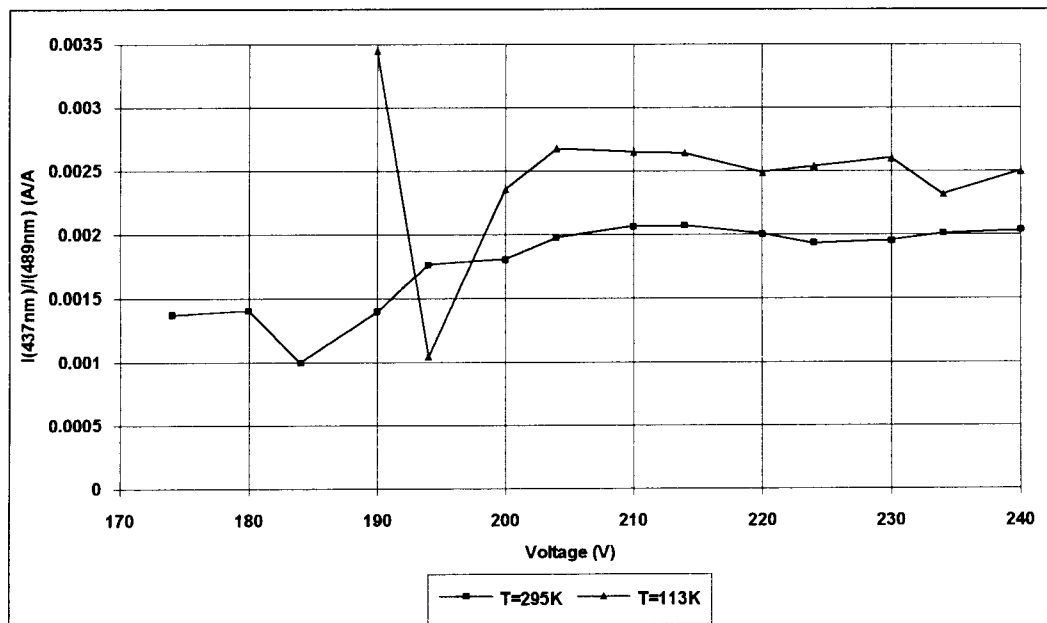


Figure 4-9. Ratio $I(437\text{nm})/I(489\text{nm})$ at $T=295\text{K}$ and $T=113\text{K}$ for the sputtered sample.

4.2.2 Discussion and Summary

No evidence for a radiative transition between the 5D_3 and the 5D_4 level is found at room temperature. Direct nonradiative transitions from these levels to the ground manifold have not been researched. Nonradiative transitions are dependent upon optical phonons. At low temperature these nonradiative transitions are reduced because of the reduction of optical phonons.

The combination of scattering and nonradiative transition rates accounts for the changes in luminescence for room and low temperature, as well as for the differences seen between ALE and sputtered samples.

The nonradiative transition rates are believed to be very important in determining the luminescence of a sample. Scattering and transition rates are different for ALE and sputtered samples because of the completely different fabrication methods. Optically this is seen in the different trends in luminescence for these samples.

The ratio of intensities, suggested by Krupka to be a method for determining the hot electron energy distribution, exhibits the same trend but is not an accurate method because of the existence of nonradiative transitions. Very low temperatures are necessary to minimize nonradiative transitions.

4.3 Field-Control Waveform Experiments

4.3.1 Room Temperature and Low Temperature Experimental Results

The voltage waveform shown in Fig. 3-2 is used to generate a constant field during part of the waveform cycle. Figure 4-10 shows the voltage waveform and the corresponding luminescence at a wavelength of 543 nm. The luminescence is very large during the portion of the waveform consisting of a succession of 28 pulses at a frequency of 10 kHz. This portion of the waveform is used to reach a steady-state interface distribution. The magnitude of the pulses appears to be less than 200V. In fact, the pulses do have a height of 210 V but, due to aliasing of the digital oscilloscope, they appear smaller. The curve also shows that sufficient time is given for the luminescence to decay completely before the field-control pulse is applied. This luminescence is studied next.

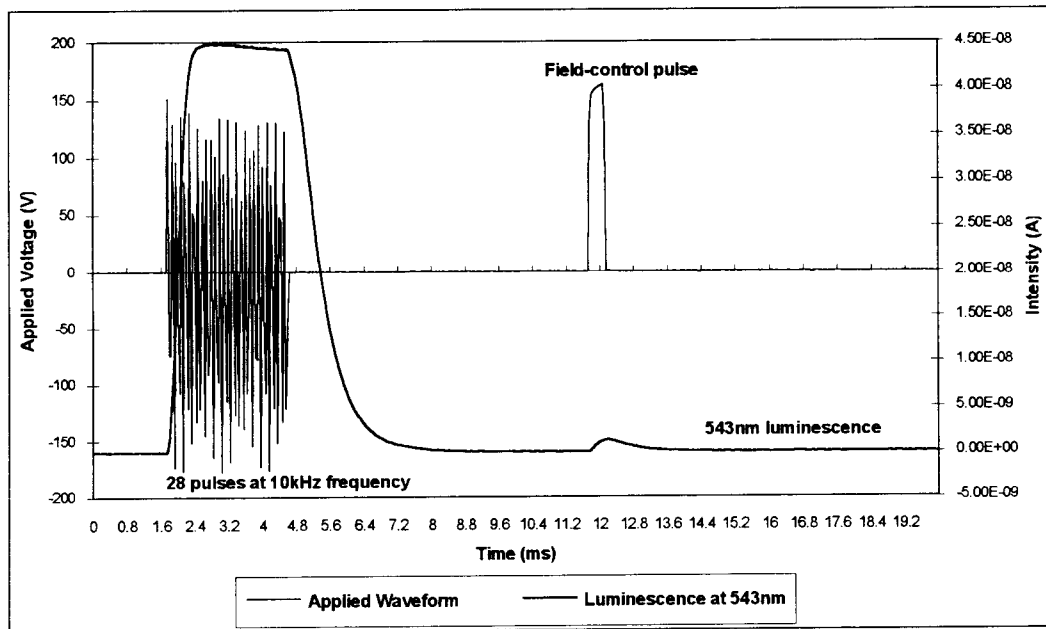


Figure 4-10. Field-control waveform and corresponding luminescence at 543 nm.

Tables 4-1 and 4-2 give a list of the capacitance values for calculating the phosphor field and internal charge for ALE and sputtered samples, respectively. Here, C_{st} is the Sawyer-Tower sense capacitor value, C_i is the insulator capacitance, C_p is the phosphor capacitance, and C_t is the total capacitance of the ACTFEL stack.

Cst	105.95	nF	
Ct	0.89	nF	T=295K
	0.8	nF	T=147K
Cp	1.23054	nF	T=295K
	1.0649	nF	T=147K
Ci	3.216	nF	
dp	6.80E-05	cm	

Table 4-1. Parameters for the ALE sample.

Cst	105.95	nF	
Ct	0.95	nF	T=295K
	0.85	nF	T=113K
Cp	1.7558	nF	T=295K
	1.44221	nF	T=113K
Ci	2.07	nF	
dp	6.80E-05	cm	

Table 4-2. Parameters for the sputtered sample.

The field-control pulse always follows a negative polarity pulse after a delay. Notice that the field-control pulse shows a slowly rising slope which ensures, in the presence of a growing opposite polarity polarization field, that the field in the phosphor remains constant (see Fig. 4-11). When selecting the height of the pulse one cannot be exactly sure what field this pulse generates. This depends on the amount of feedback from

the sense capacitor. The voltage on the sense element is dependent on the sample and the temperature. Therefore the maximum voltage of the field-control pulse is recorded and the corresponding field is determined after the measurement is taken.

For the ALE sample, it can be seen that the fields are very constant during the application of the field-control pulse, indicating that the circuit is working well. The lowest field of 0.6 MV/cm is achieved when the maximum voltage on the field-control pulse is 50 V. The largest field achieved at room temperature is 1.82 MV/cm at a maximum applied voltage of 240 V, at $T=147$ K the largest field is 2.14 MV/cm at an applied voltage of 250 V. The phosphor fields at room and low temperature are shown in Figs. 4-12 and 4-13, respectively. The conversion from pulse voltage to phosphor field using Eqn. 2-12 is shown in Table 4-3.

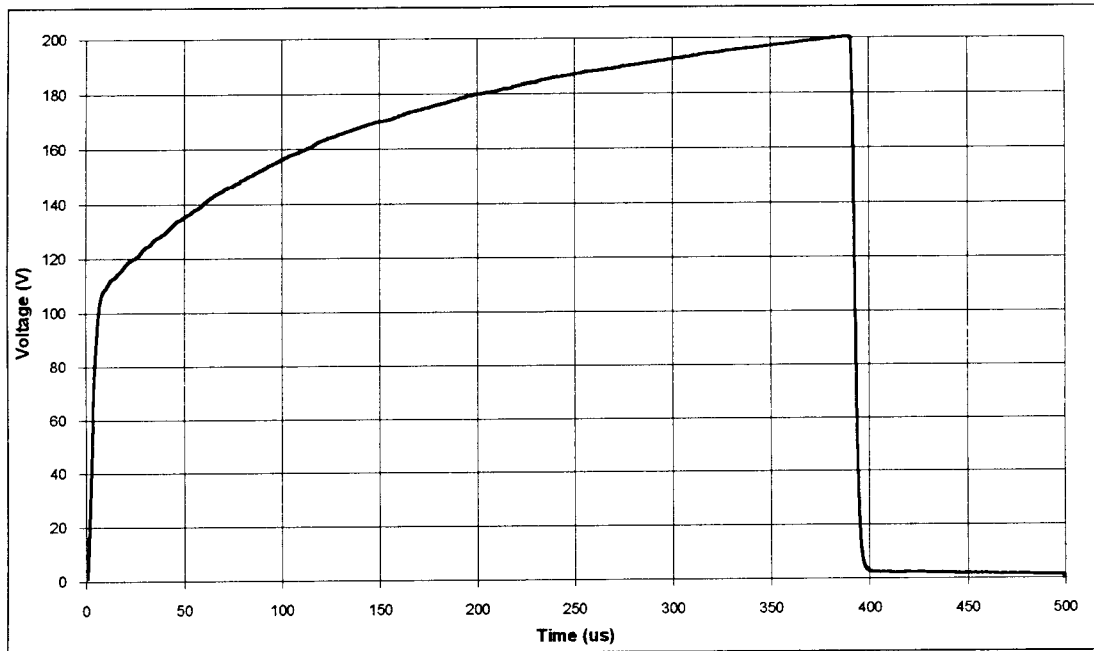


Figure 4-11. Example of a field control pulse.

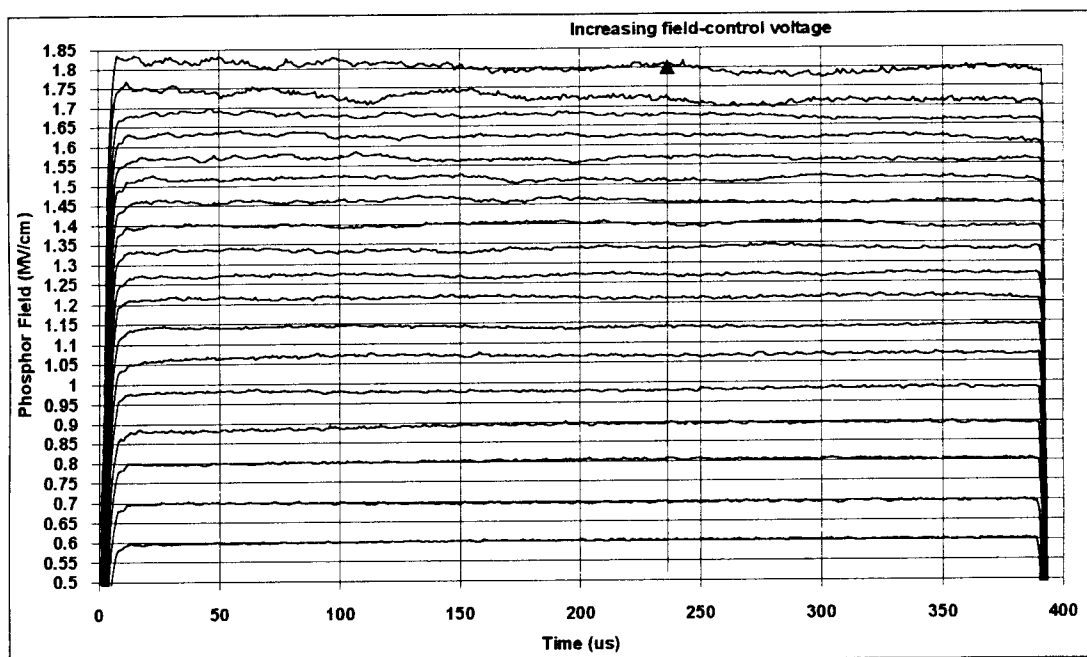


Figure 4-12. Phosphor fields at T=295 K for the ALE sample.

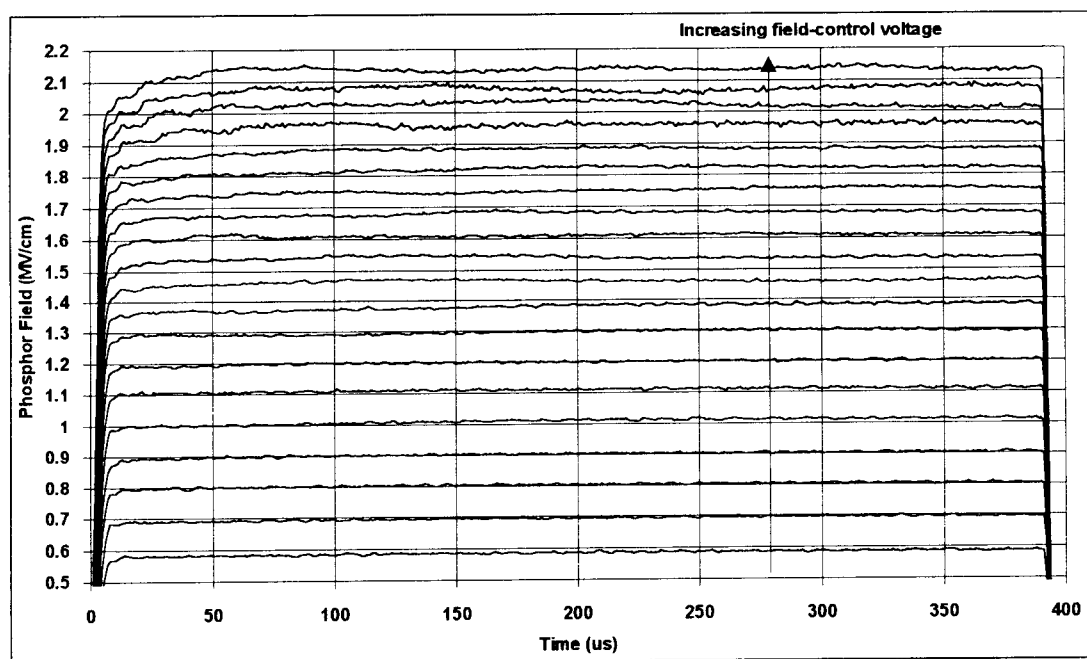


Figure 4-13. Phosphor fields at T=147 K for the ALE sample.

T=295K		T=147K	
Voltage	Field	Voltage	Field
(V)	(MV/cm)	(V)	(MV/cm)
50	0.6	50	0.6
60	0.7	60	0.7
70	0.8	70	0.8
80	0.88	80	0.9
90	0.98	90	1
100	1.07	100	1.11
110	1.14	110	1.2
120	1.22	120	1.3
130	1.27	130	1.37
140	1.33	140	1.46
150	1.4	150	1.53
160	1.46	160	1.61
170	1.52	170	1.68
180	1.57	180	1.75
190	1.63	190	1.82
200	1.67	200	1.88
220	1.72	220	1.95
240	1.82	230	2.02
		240	2.07
		250	2.14

Table 4-3. Conversion from applied voltage to phosphor field in the ALE sample.

The phosphor fields generated in the sputtered sample show fluctuations at higher fields at room temperature. It is believed that micro breakdowns in the BTO insulators are the cause of these fluctuations. At low temperature these fluctuation are less evident and constant phosphor fields up to 1.65 MV/cm are achieved. Overall, since sputtered samples are much more fragile and easier to burn out, it is not possible to go to very high phosphor fields. Especially at room temperature there seems to be a problem in generating constant fields. More work needs to be done to improve the existing conditions. The lowest fields of 0.67 MV/cm at room temperature and 0.72 MV/cm at T=113 K are achieved when the maximum voltage on the field-control pulse is 90 V. The

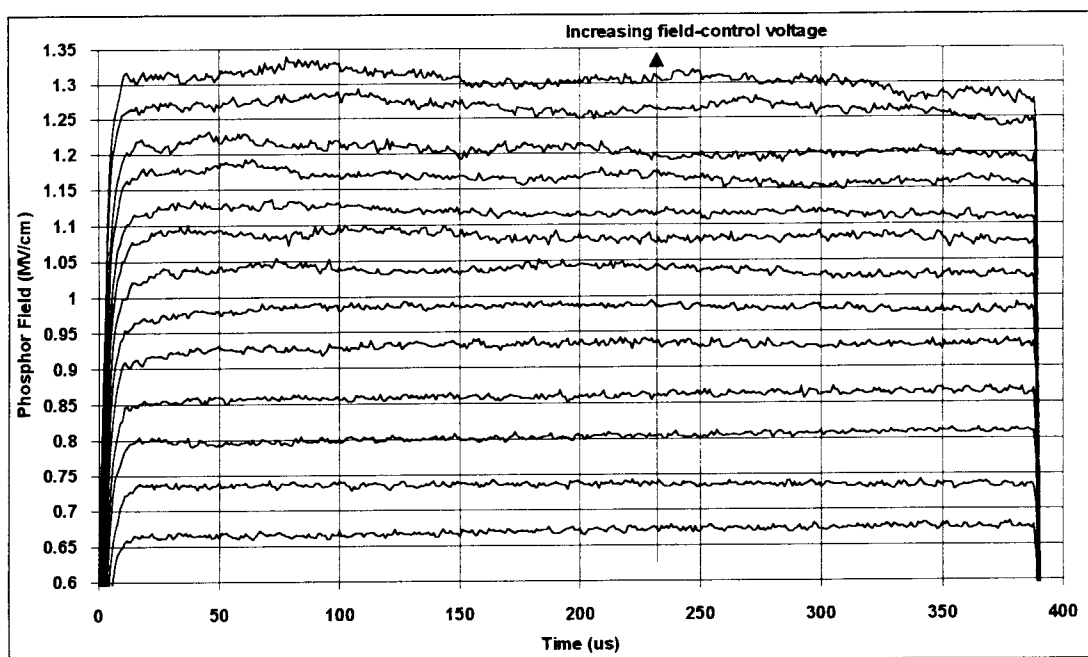


Figure 4-14. Phosphor fields at $T=295$ K for the sputtered sample.

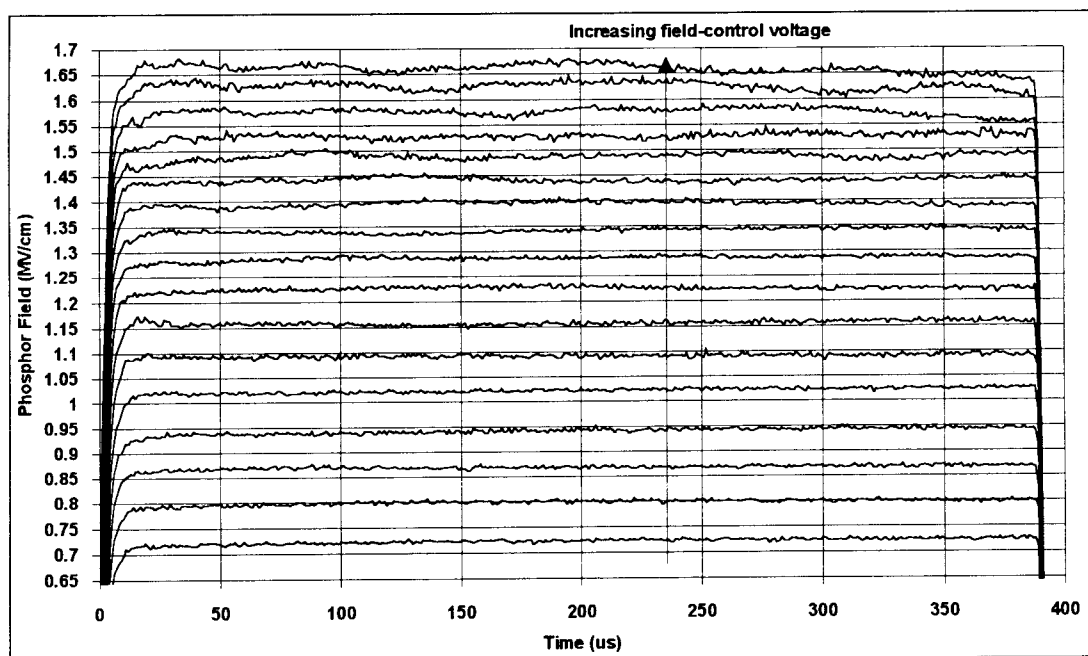


Figure 4-15. Phosphor fields at $T=113$ K for the sputtered sample.

largest field achieved at room temperature is 1.32 MV/cm at a maximum applied voltage of 220 V, at T=113 K the largest field is 1.66 MV/cm at 250 V applied voltage. The phosphor fields at room and low temperature are shown in Figs. 4-14 and 4-15, respectively. The conversion from pulse voltage to phosphor field using Eqn. 2-11 are shown in Table 4-4.

T=295K		T=135K	
Voltage	Field	Voltage	Field
(V)	(MV/cm)	(V)	(MV/cm)
90	0.67	90	0.72
100	0.73	100	0.8
110	0.8	110	0.87
120	0.86	120	0.94
130	0.93	130	1.02
140	0.98	140	1.09
150	1.03	150	1.16
160	1.08	160	1.23
170	1.12	170	1.28
180	1.17	180	1.34
190	1.21	190	1.39
210	1.27	200	1.44
220	1.32	210	1.48
		220	1.53
		230	1.57
		240	1.63
		250	1.66

Table 4-4. Conversion from applied voltage to phosphor field in the sputtered sample.

Figures 4-16 and 4-17 show the internal charge for the ALE sample, as do Figs. 4-18 and 4-19 for the sputtered sample. The internal charge is the charge moving across the phosphor as a function of time, the conduction charge is the total amount of charge transferred from one insulator/phosphor interface to the other while a voltage pulse is

applied, and the polarization charge is the total remaining charge present when no voltage pulse is applied.

From Figs. 4-16 and 4-17, it is seen that the larger the applied field, the larger the conduction current. Obvious changes are seen when comparing the internal charge at room temperature and low temperature. For the same phosphor field applied, the amount of charge transferred from one side to the other is larger at room temperature. The conduction charge depends on the polarization charge present in the phosphor. The internal charge changes with temperature, thus changing the polarization charge. Less charge is transferred inside the phosphor at low temperature. The phosphor field is a function of the internal charge. Equations 2-7 and 2-11 show the internal charge dependence of the phosphor field. For a given external voltage applied in the form of a pulse, the resulting field is larger if the internal charge is smaller. This shows why at lower temperature the fields are larger for the same applied field-control voltage pulse.

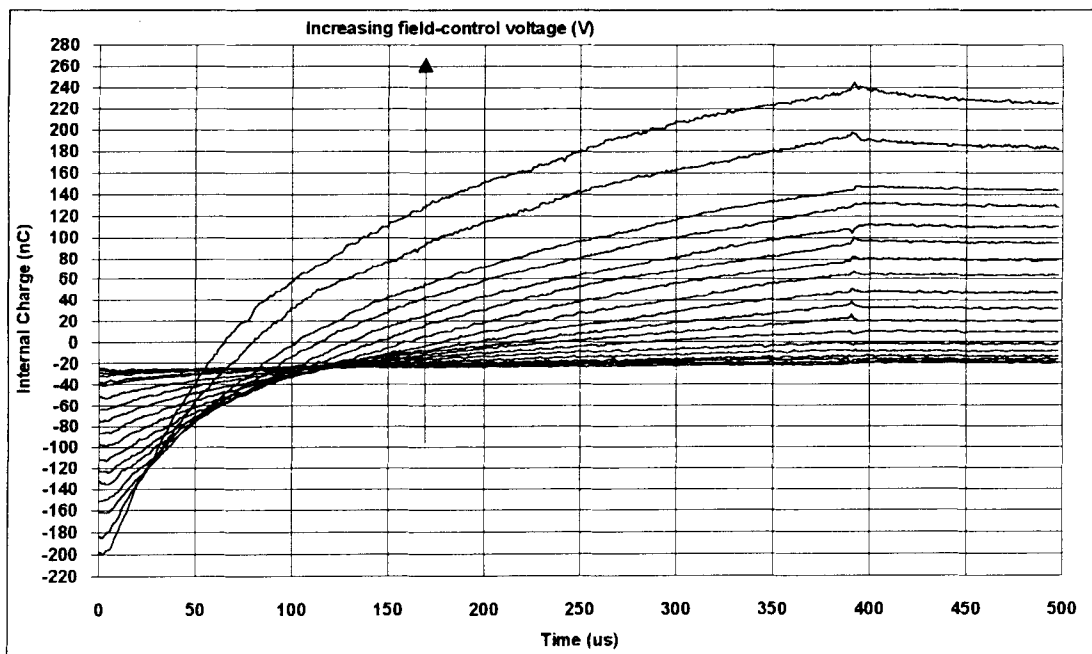


Figure 4-16. Internal charge at $T=295$ K for the ALE sample.

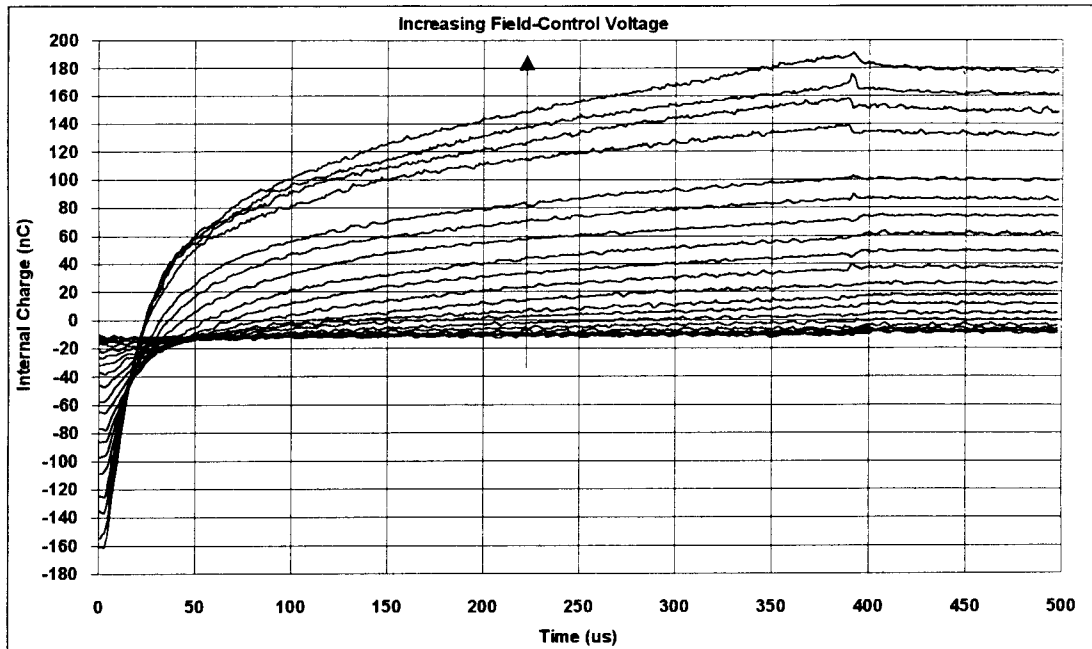


Figure 4-17. Internal charge at $T=147$ K for the ALE sample.

For the sputtered samples, the same trend is seen as with the ALE samples. The internal charge at a given temperature rises as the phosphor field is increased. At lower temperature less charge is present than at room temperature under same field conditions.

One obvious difference of internal charge between sputtered and ALE samples is the rate of charge transfer from one insulator/phosphor interface to the other. In sputtered samples the rate of transfer of charge across the phosphor is nearly constant (see Figs. 4-18 and 4-19). In ALE samples, more charge is transferred during the early part of the field-control pulse and less towards the end of it (see Fig. 4-16 and 4-17).

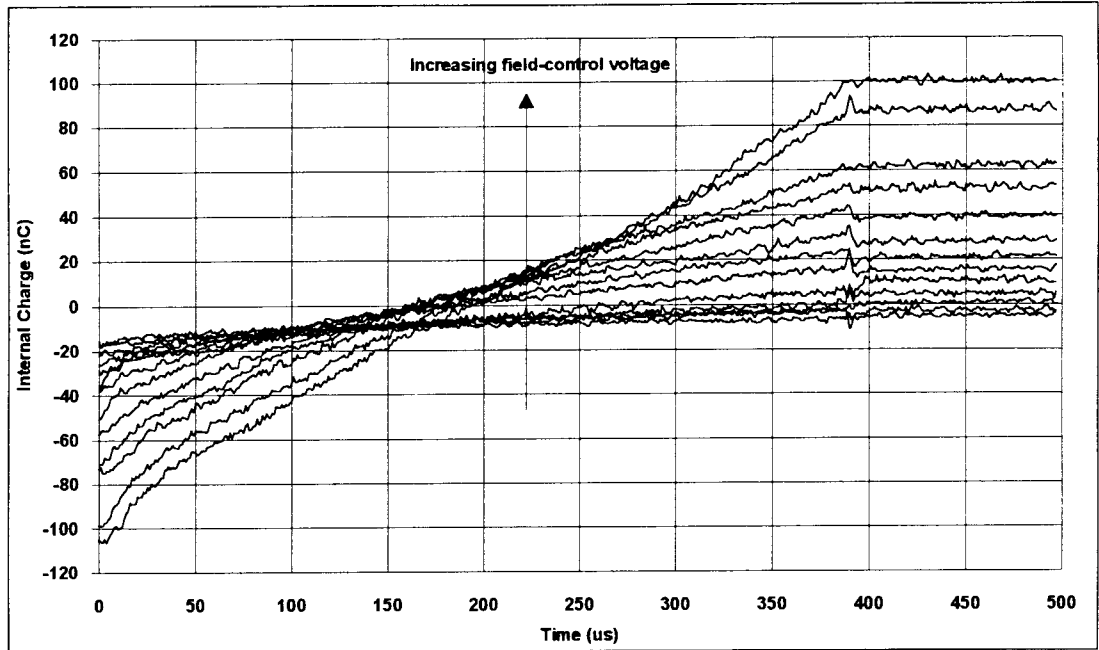


Figure 4-18. Internal charge at $T=295$ K for the sputtered sample.

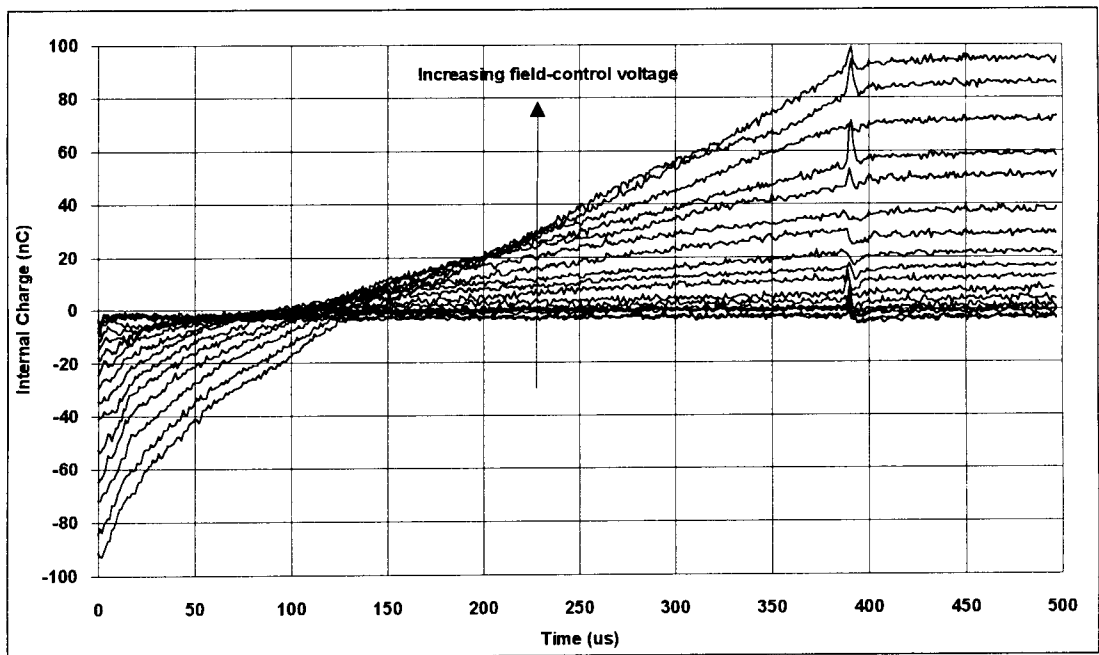


Figure 4-19. Internal charge at $T=113$ K for the sputtered sample.

The $Q-F_p$ curves for the field-control pulse are shown in Figs. 4-20 and 4-21 for the ALE sample and in Figs. 4-22 and 4-23 for the sputtered sample. $Q-F_p$ curves for each phosphor field are plotted in order to make sure that field clamping does occur. The $Q-F_p$ curves also provide information on the conduction charge for each phosphor field. The curves need to be observed in a clockwise manner. The beginning of the field-control pulse starts at the lower right portion of the curve, then continues in a clockwise manner, through the full pulse.

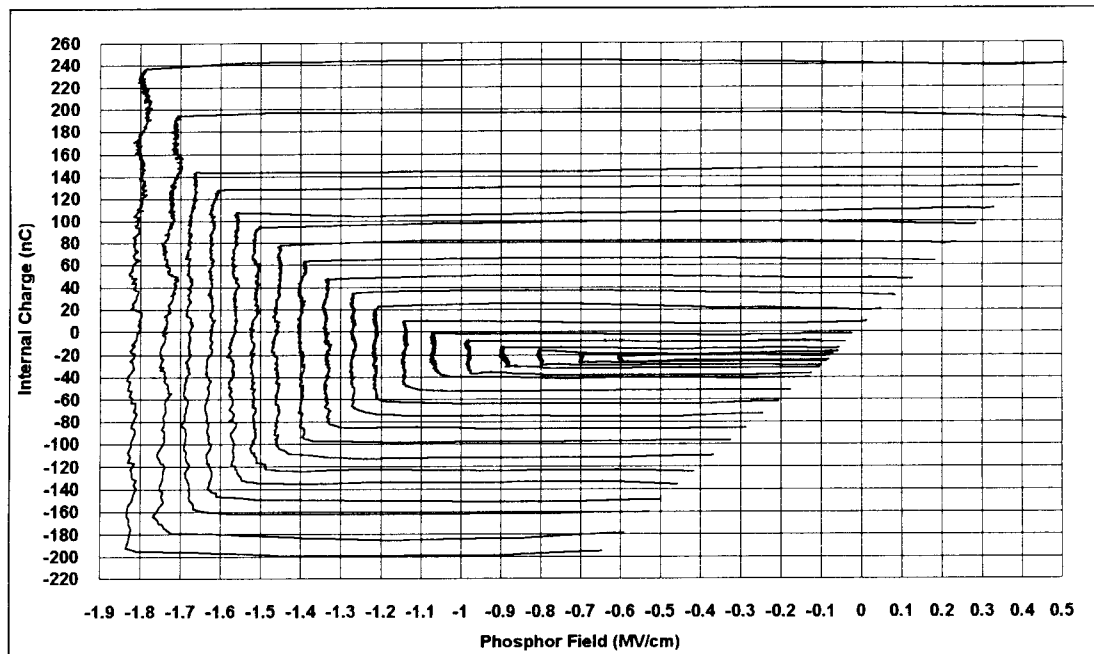


Figure 4-20. $Q-F_p$ curves at $T=295$ K for the ALE sample.

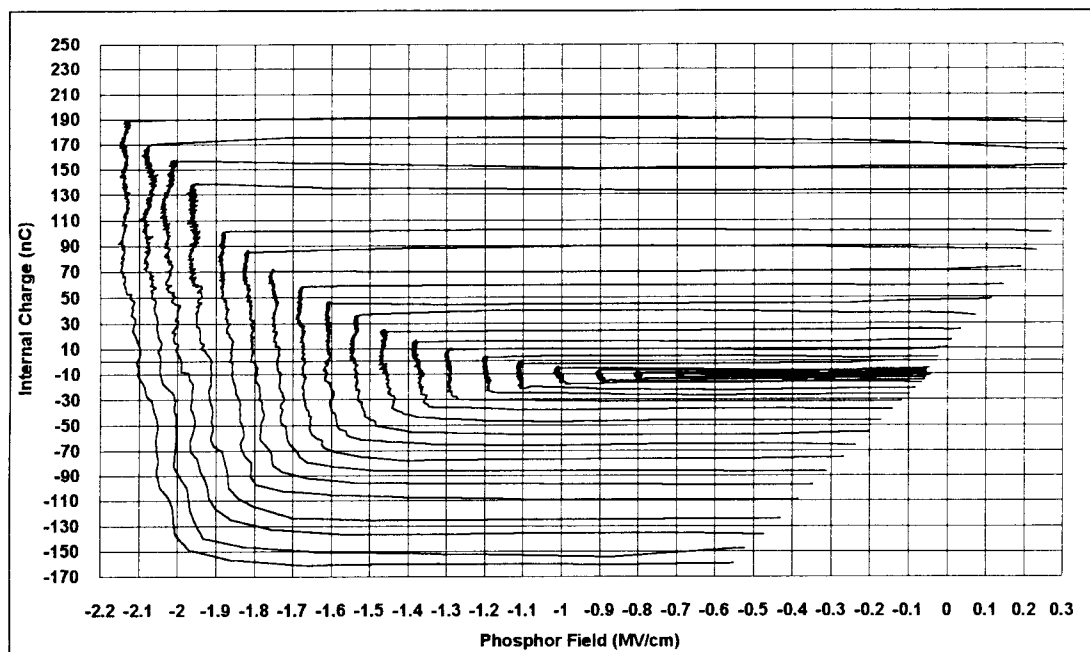


Figure 4-21. Q-F_p curves at T=147 K for the ALE sample.

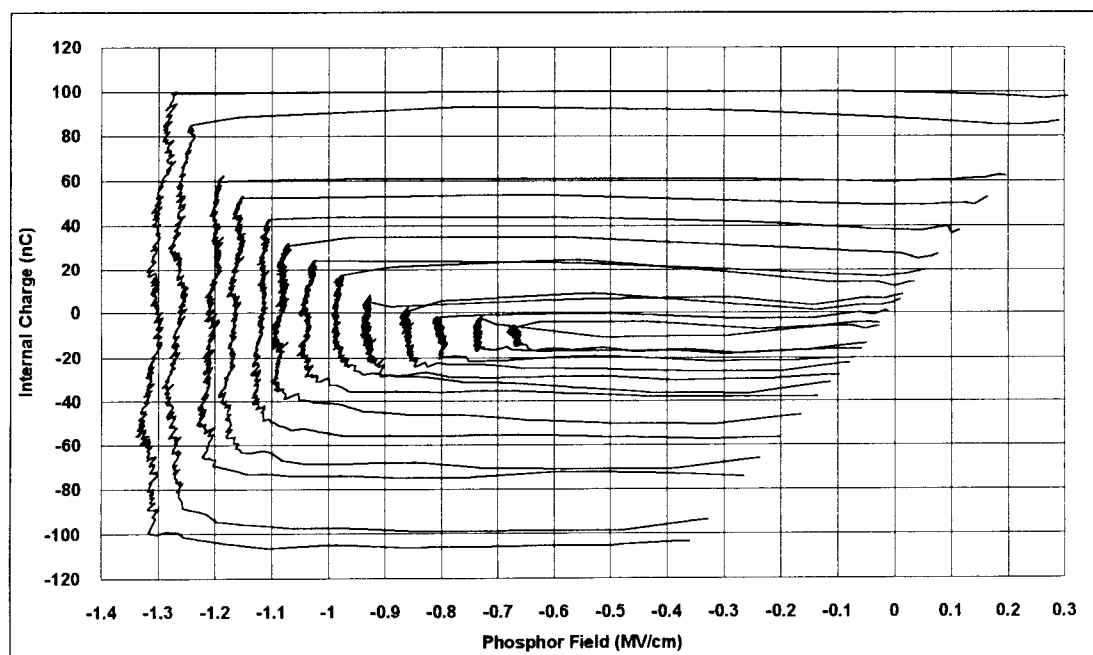


Figure 4-22. Q-F_p curves at T=295 K for the sputtered sample.

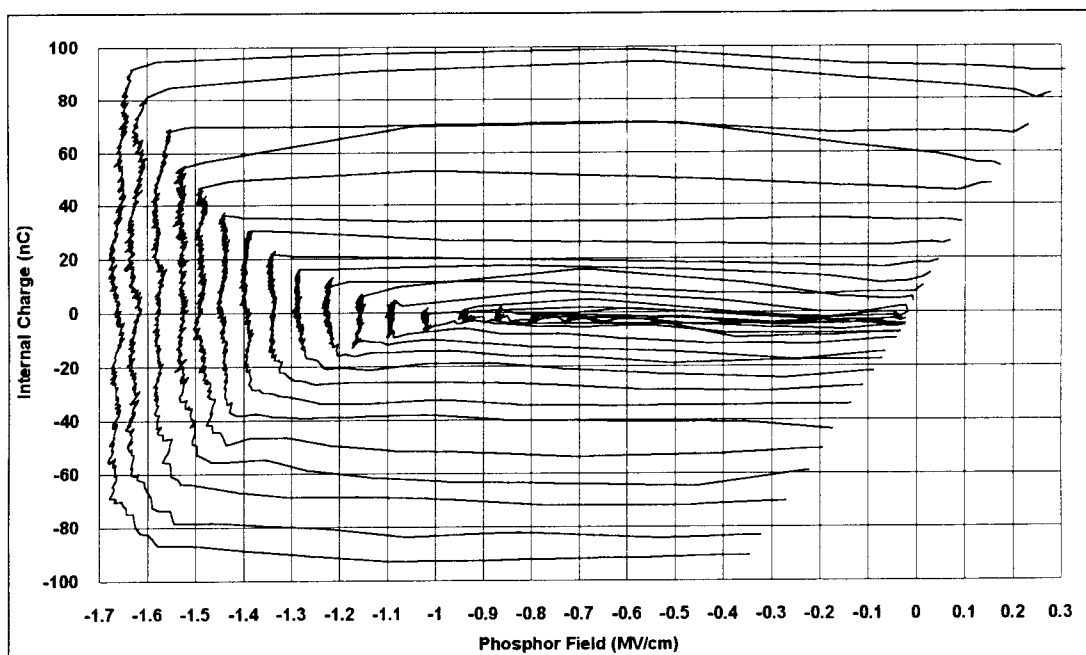


Figure 4-23. Q - F_p curves at $T=113$ K for the sputtered sample.

The conduction charge is found by monitoring the amount of charge transferred when the field-control pulse is applied. On the Q - F_p curves the conduction charge is simply the total change in charge when the field is clamped.

Initially, the Q - F_p curves for both temperatures showed a slight slant before and after the field-clamping portion. When monitoring the internal charge as a function of time (see Figs. 4-16 through 4-19), a sudden drop in charge could be seen at the end of the field-control pulse. Physically, this phenomenon makes no sense since it implies that charge is lost rapidly at the end of the field-control pulse. This does not happen because the polarization charge does not suddenly vanish.

When the field applied by the field-control pulse is very high, a significant amount of polarization charge remains. This charge generates a field on the order of 0.5 MV/cm. This field is large enough for some of the electrons in the interface states to be injected

into the conduction band and be accelerated toward the opposite insulator/phosphor interface, even though no external bias is applied (this charge is denoted leakage charge). Therefore, there is a slow decrease in polarization charge. In order to lose all the polarization charge to leakage, several tens of milliseconds (or longer) must pass. A sudden loss of charge, as seen in the $Q-F_p$ curve is not possible.

The slant in the $Q-F_p$ curve is due to the incorrect value of the total capacitance C_t of the stack. C_t is estimated from the $C-V$ curve to be 0.8 nF. The internal charge, obtained in a $Q-F_p$ measurement, is dependent on the value of C_t . Choosing the correct value of C_t eliminates the slant in the $Q-F_p$ curve. But, when moving to lower temperature, the same slant on the $Q-F_p$ curve shows up again. The reason is that C_t is also a function of temperature. C_t is equal to the insulator and phosphor capacitances in series. It has been established [25] that C_t does not change very much with temperature, so the change in C_t is due to a change in C_p .

In Eqn. 2-5, the dependence of the internal charge on C_p can be seen. Knowing that C_p changes with temperature the following simulations are undertaken. C_p is varied slightly above and below its estimated value and the corresponding $Q-F_p$ and $q(t)$ curves are observed. This procedure is an excellent guideline for determining the correct C_p value. Figures 4-24 and 4-25 show the $q(t)$ and $Q-F_p$ variations, respectively, with changing C_p . When the phosphor capacitance is overestimated, a reduction in internal charge occurs during the field-control pulse. At the end of the field-control pulse a sudden increase in charge is seen (see Fig. 4-24). As was mentioned before, this result is unphysical. If the phosphor capacitance is underestimated, the opposite trend occurs. During the field-control pulse, the charge is shifted higher while at the end of it a sudden drop in charge is observed. The correct value of C_p results in no loss of charge at the end of the field-control pulse. When observing the $Q-F_p$ plot, including the over- and underestimation of the phosphor capacitance, one can see that the phosphor field itself is not affected but a slant in the curve occurs before and after the field-clamping.

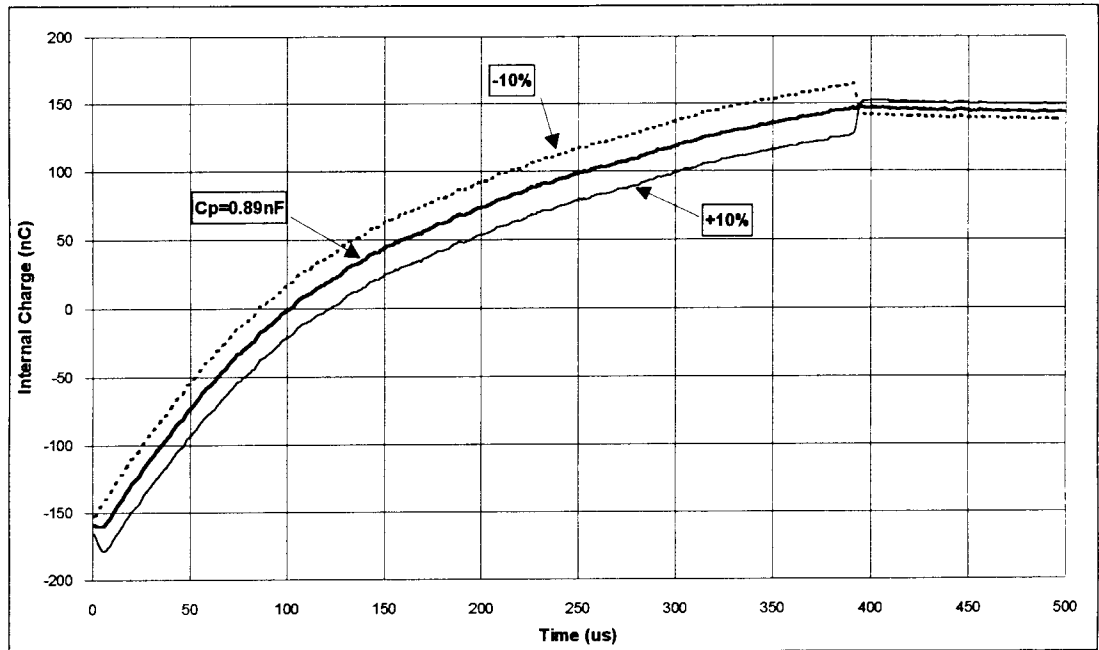


Figure 4-24. Internal charge $q(t)$ versus time with variations in C_p .

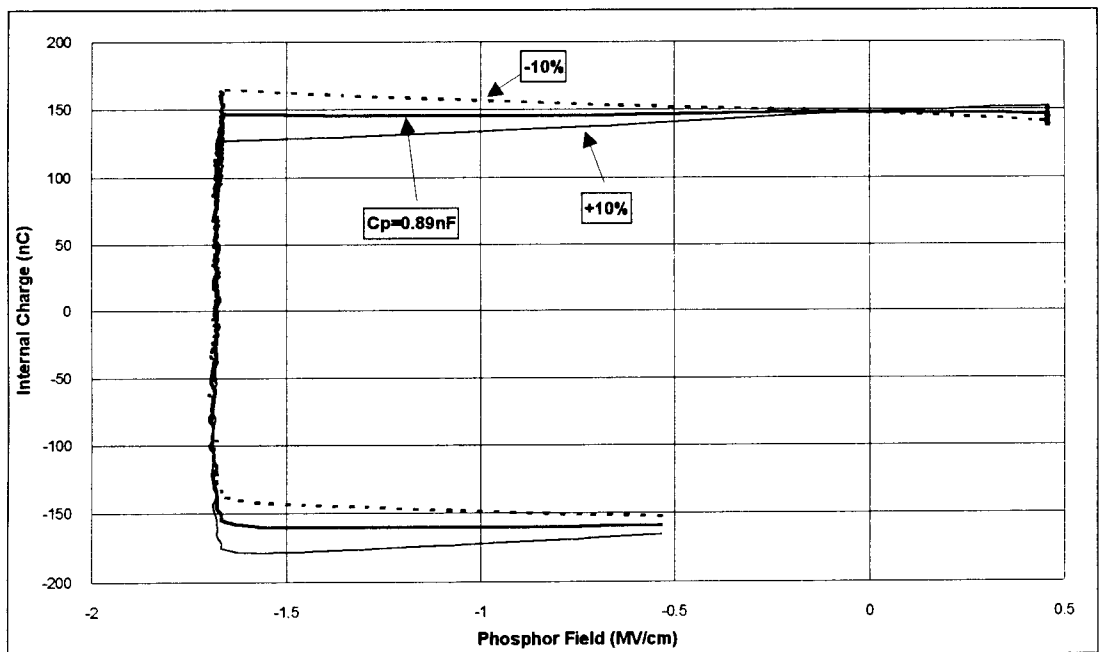


Figure 4-25. $Q-F_p$ with variations in C_p .

The luminescence for the ALE sample at wavelengths 437 nm, 489 nm, and 543 nm are shown in Figs. 4-26, 4-27, and 4-28, respectively. The luminescence for the sputtered sample at the same wavelengths are shown in Figs. 2-29, 4-30, and 4-31, respectively.

The luminescence curves for the ALE sample show a dramatic increase at lower temperature. For large fields the increase is most pronounced at the wavelength of 437 nm which corresponds to luminescence from the $^5D_3-^7F_4$ transition.

In contrast, the luminescence curves for the sputtered sample all show a decrease in intensity at lower temperature.

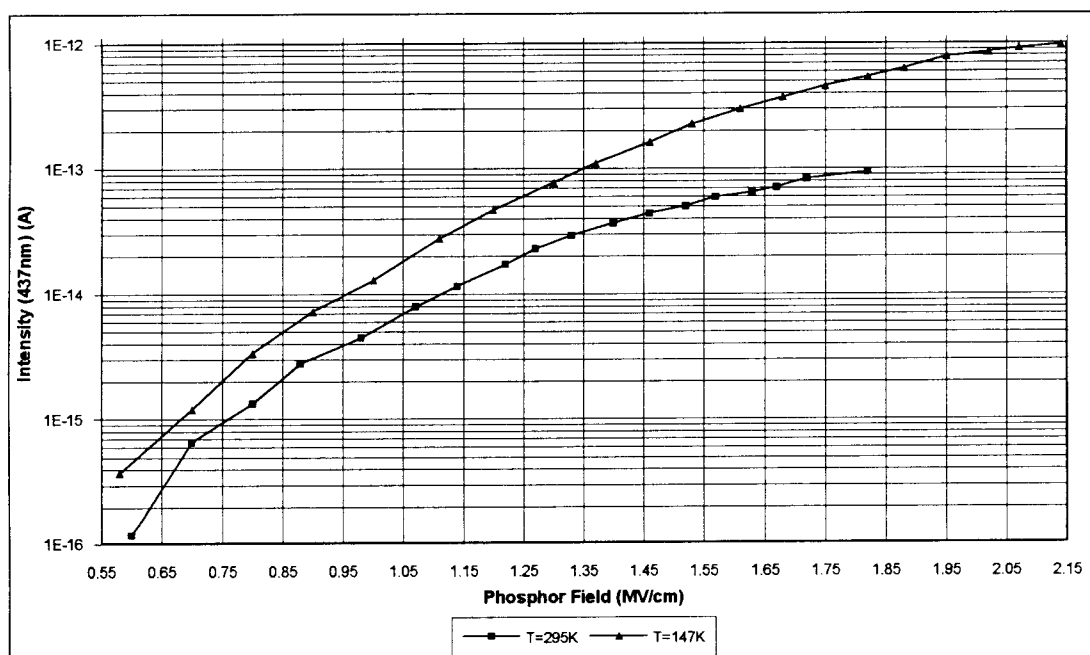


Figure 4-26. Intensity at 437 nm for T=295 K and T=147 K for the ALE sample.

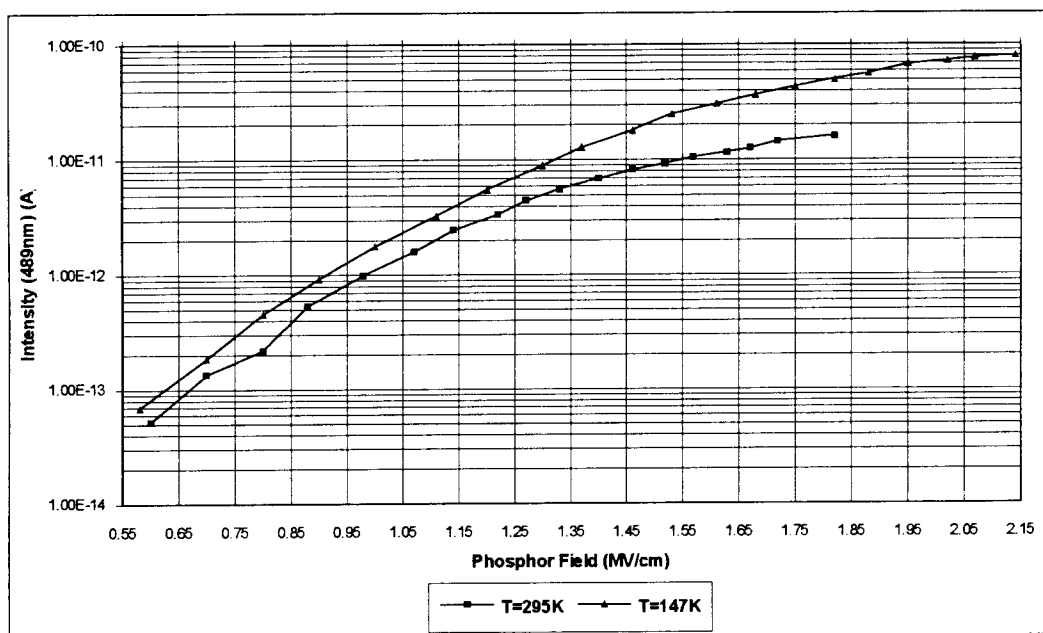


Figure 4-27. Intensities at 489 nm for T=295 K and T=147 K for the ALE sample.

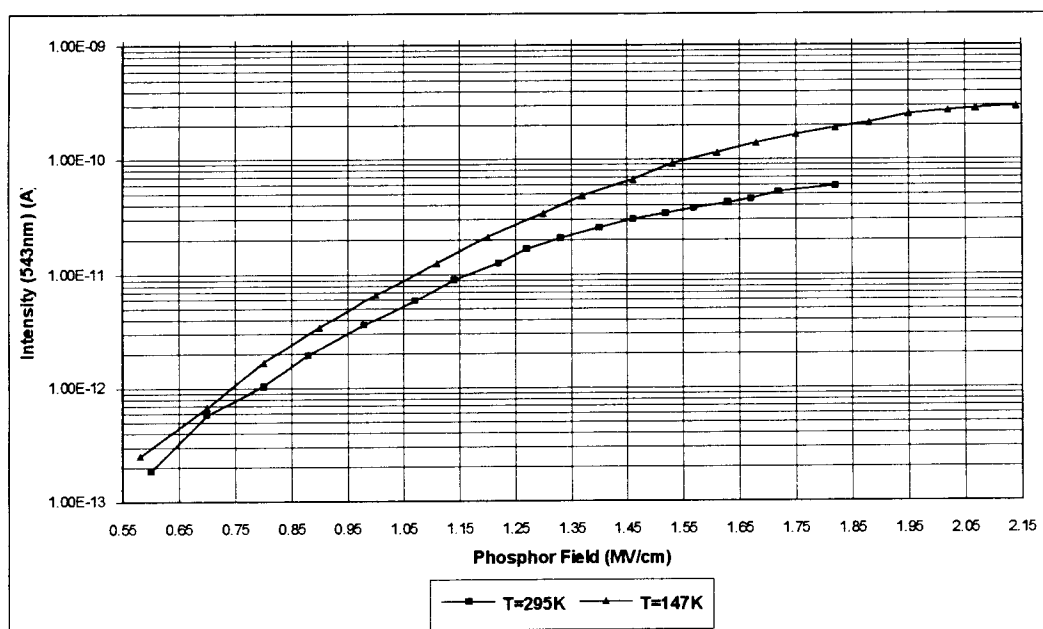


Figure 4-28. Intensities at 543 nm for T=295 K and T=147 K for the ALE sample.

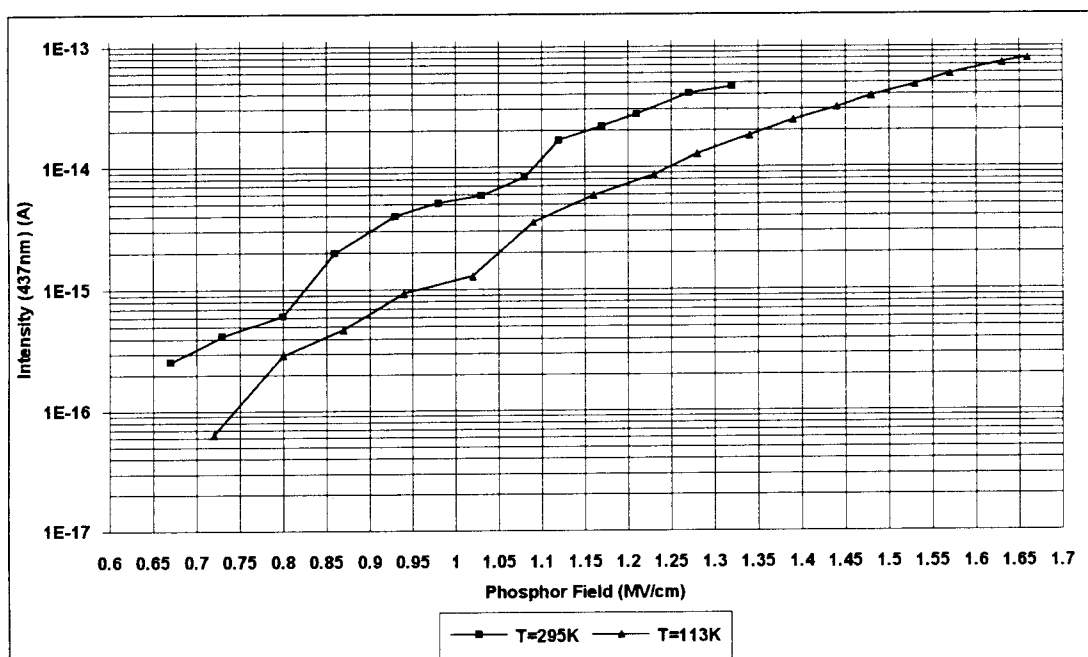


Figure 4-29. Intensities at 437 nm for T=295 K and T=113 K for the sputtered sample.

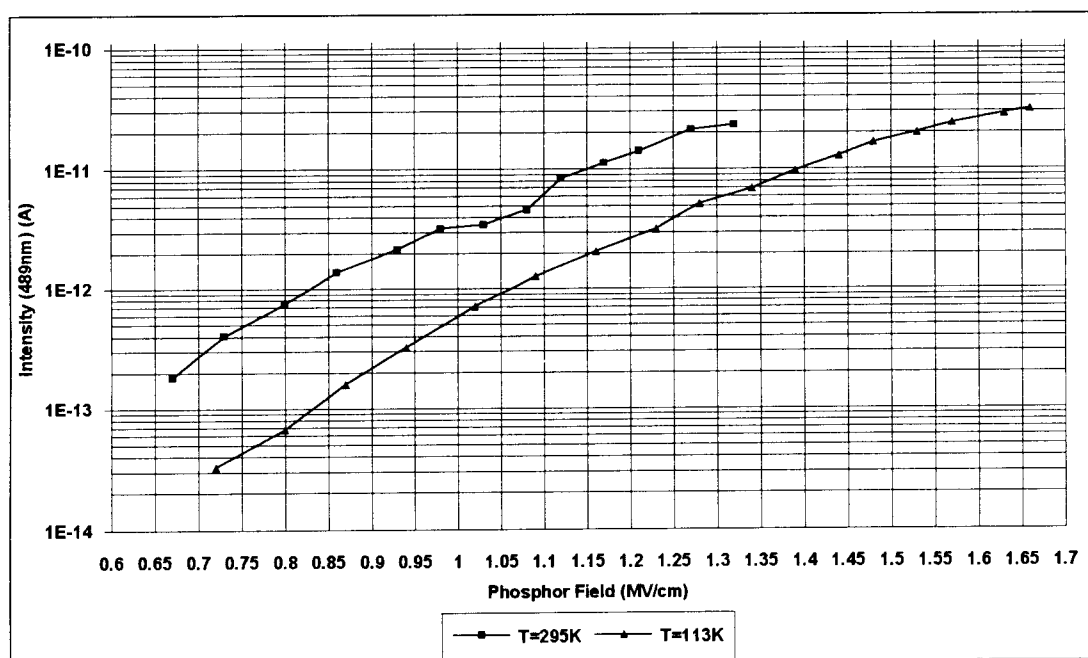


Figure 4-30. Intensities at 489 nm for T=295 K and T=113 K for the sputtered sample.

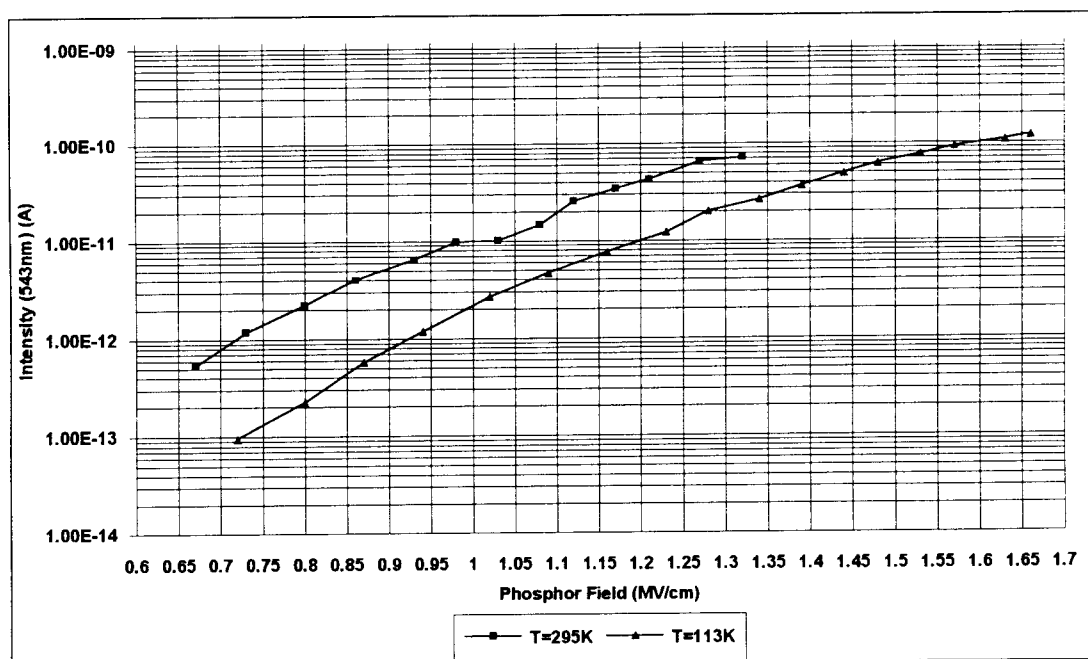


Figure 4-31. Intensities at 543 nm for T=295 K and T=113 K for the sputtered sample.

Following the method suggested by Krupka of plotting peak intensity ratio versus applied voltage, or in this case the controlled electric field, Figs. 4-32 and 4-33 show the intensity ratios of the 437 nm and 489 nm emission peaks for the ALE and the sputtered sample, respectively, at room and low temperature. The ALE sample shows an increase and saturation in the ratio for both low and room temperature, suggesting a heating of the electron distribution for increasing phosphor fields, but the trend is not nearly as clear as in Krupka's experiment. The sputtered sample shows the same general trend, although the data is quite erratic at low fields. The trends in these curves agree with the results obtained by Krupka [9], but it is hard to draw much of a conclusion because the trends are fairly obscure. One possible reason for this is that nonradiative decay between levels is clouding the radiative emission results. Only by making changes to the cooling of the

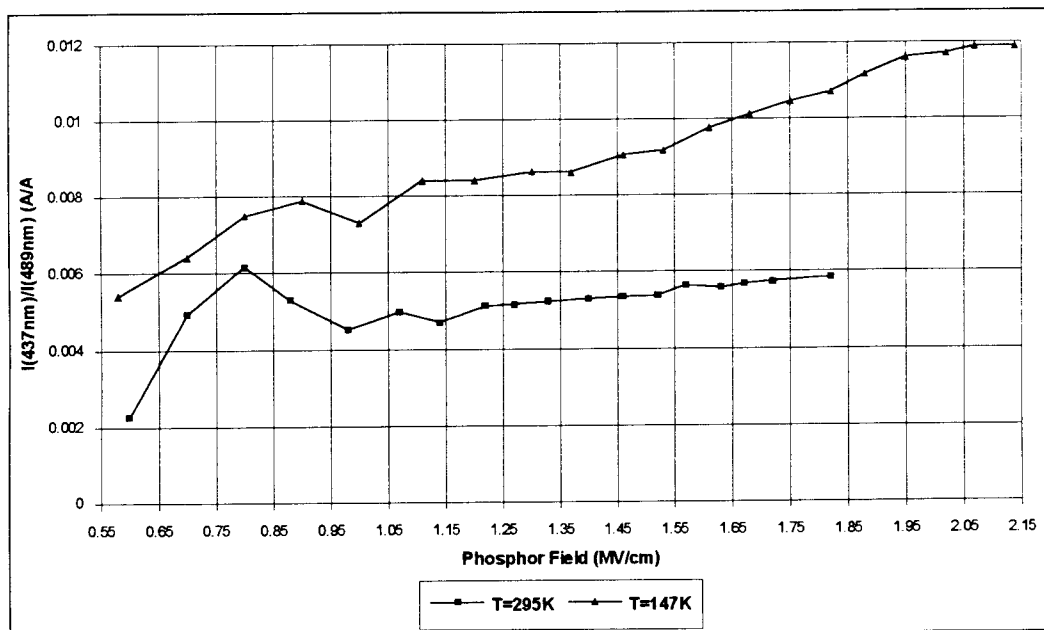


Figure 4-32. Ratio of $I(437\text{nm})/I(489\text{nm})$ for $T=295\text{K}$ and $T=147\text{K}$ for the ALE sample.

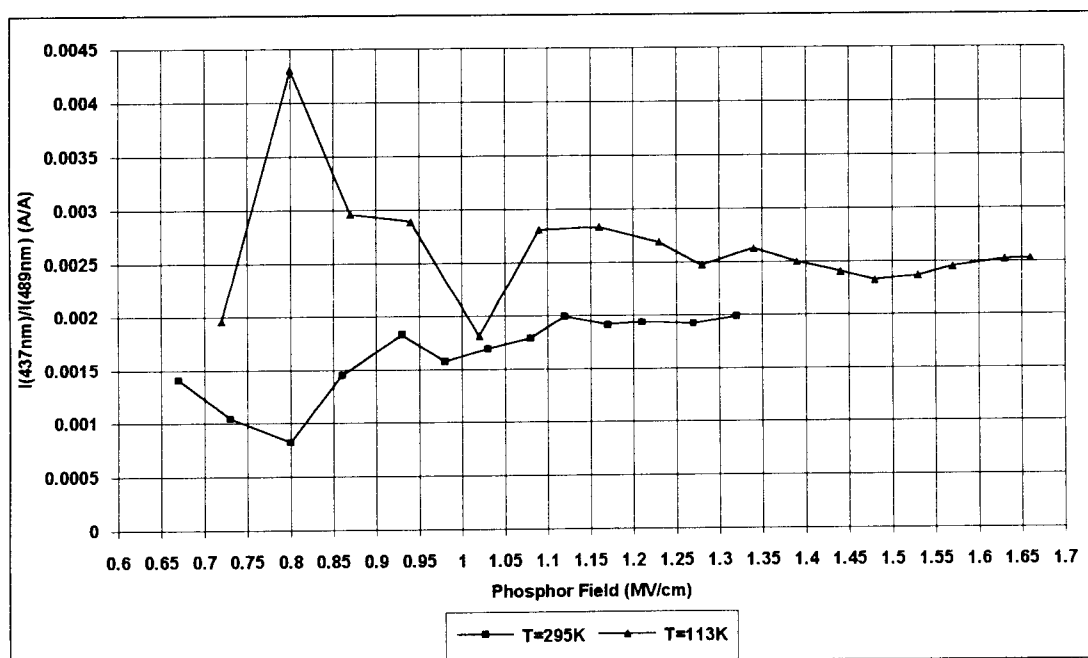


Figure 4-33. Ratio of $I(437\text{nm})/I(489\text{nm})$ for $T=295\text{K}$ and $T=113\text{K}$ for the sputtered sample.

sample to achieve 77 K samples as Krupka used, will we be able to eliminate many nonradiative effects and compare the field-control results to his.

Perhaps a better way to examine this data is to look at the emission efficiency per conducted electron, i.e. a normalized output or efficiency. Figures 4-34 and 4-35 show the intensity at a wavelength of 489 nm normalized with respect to the conduction charge, taken from the Q - F_p curves, for the ALE and sputtered samples, respectively. Both room and low temperature curves are displayed. This normalized intensity is called the "quantum yield" of the Tb impact excitation and can be directly compared to the results obtained by Monte Carlo simulations. In Monte Carlo simulations the number of excitations per number of electrons injected versus phosphor field can be found.

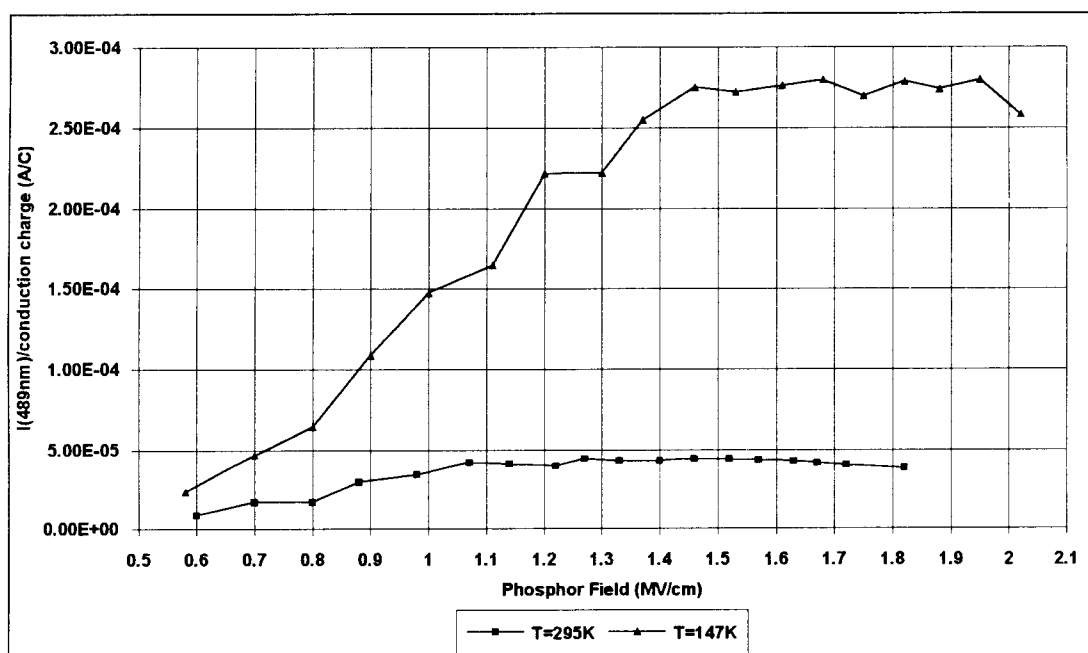


Figure 4-34. Normalized intensity at 489 nm at $T=295$ K and $T=147$ K for the ALE sample.

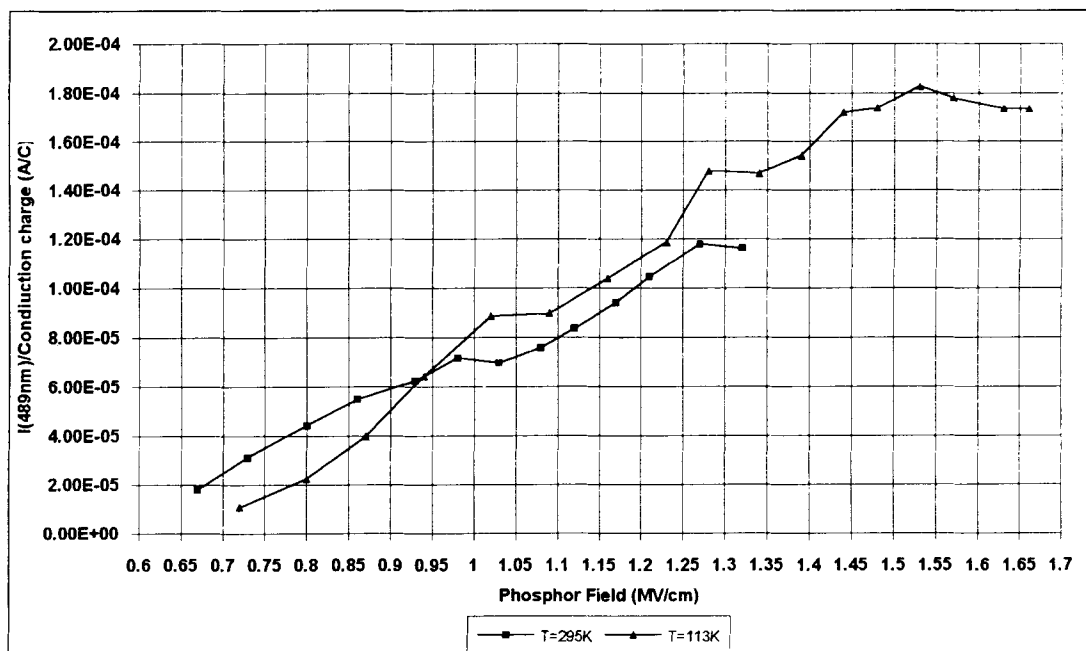


Figure 4-35. Normalized intensity of 489 nm at T=295 K and T=113 K for the sputtered sample.

The Tb impact excitation quantum yield can be compared directly to the normalized intensity shown here. Here in Figs. 4-34 and 4-35 the intensity divided by the conduction charge is directly related to the number of excitations divided by the number of injected electrons. The intensity is proportional to the number of excitations and the conduction charge is a measure of the electrons traversing the phosphor. Figure 4-36 shows room and low temperature quantum yield curves for the ALE and sputtered samples on the same curve.

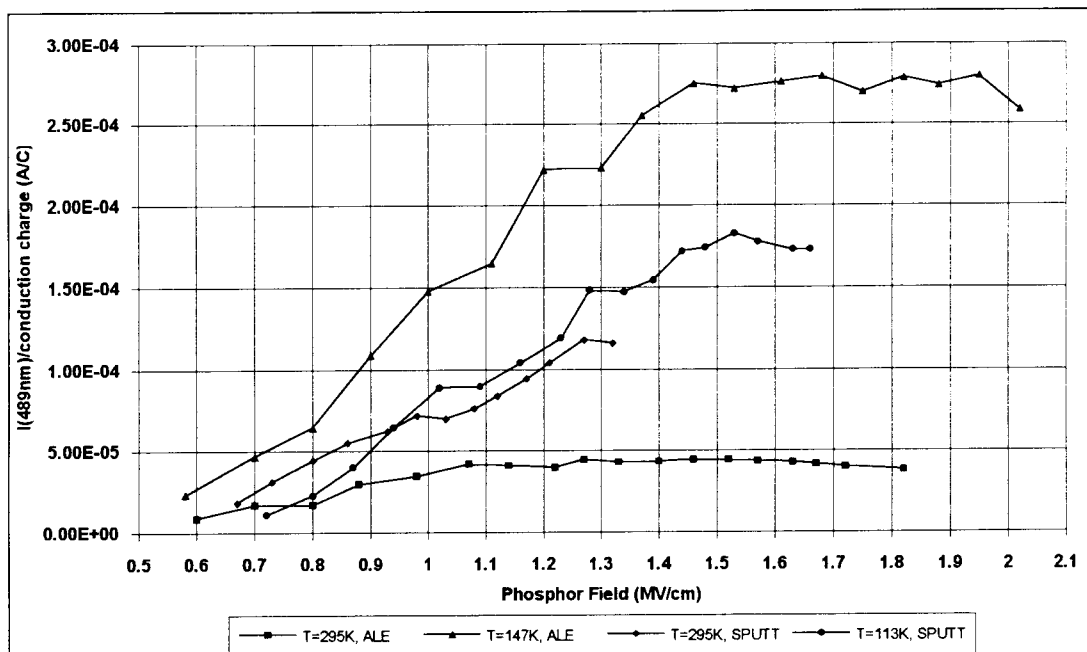


Figure 4-36. Normalized intensity of 489 nm for the ALE and the sputtered sample.

Figure 4-36 shows that the quantum efficiency of the sputtered sample hardly changes with temperature, while the ALE sample shows an increase in efficiency at lower temperature. At room temperature the efficiency for the ALE sample is much less than for the sputtered sample, whereas at low temperature the ALE efficiency is much larger than for sputtered. This shows that in the ALE sample there exists a mechanism which controls the efficiency of the EL device and which is temperature dependent.

With these curves, a direct comparison can be made between the simulation of phosphors and the experimental results. Figure 4-37 shows the curve obtained by Monte Carlo simulation, by Shankar Pennathur in our department. The plot shows both the Tb impact excitation quantum yield as well as the impact ionization quantum yield. The impact excitation quantum yield (or efficiency) is compared to the room temperature experimental data for the ALE and the sputtered sample. The trend is the same both for

simulation and experiment. There is a steady increase in normalized intensity, meaning that more and more excitations take place with respect to the number of electrons injected into the phosphor via interface states. In the experiment saturation occurs at around 1.5 MV/cm for room temperature and low temperature. According to the Monte Carlo simulation saturation occurs around 2 MV/cm for room temperature. Low temperature Monte Carlo simulations for ZnS:Tb have not yet been studied. Even though the onset of saturation differs between experiment and simulation, the trend is definitely the same. Saturation is believed to be due to the rapid increase in band-to-band impact ionization which competes with the impact excitation of terbium ions. As can be seen in Fig. 4-37, when the rate of impact ionization reaches a critical value, the Tb impact excitation quantum yield start to saturate.

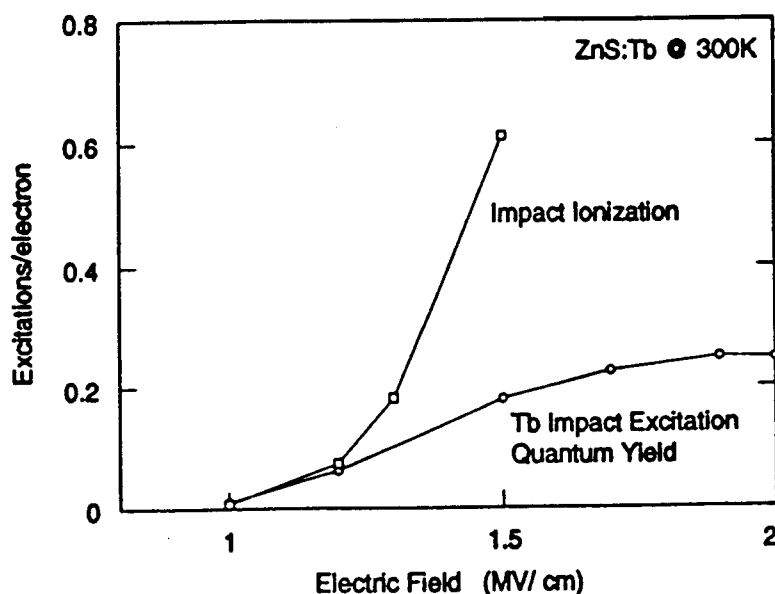


Figure 4-37. Internal quantum yield for terbium impact excitation and ionization as a function of the phosphor field in ZnS:Tb

4.3.2 Discussion and Summary

The field-control circuitry works very well for the ALE sample in establishing constant fields, both at room and low temperature. Minor fluctuations do take place at high field strengths. With the sputtered sample, large fluctuations occur at room temperature when applying large phosphor fields. The cause for these fluctuations is not known but must be related to the sputtered sample itself because the ALE sample does not exhibit these fluctuations. A possible explanation could be instabilities caused from micro breakdowns of the sputtered BTO insulators which are known to be inferior to the ALE ATO insulators. One could make samples with better insulators to verify this hypothesis.

Much information can be gained by inspecting the internal charge transfer during the field-control pulse. The total capacitance needs to be known in order to obtain accurate and meaningful results. One way to obtain the real value of the total capacitance is to observe the internal charge and the $Q-F_p$ graphs while the field-control pulse is set. A sudden drop or increase in charge at the end of the pulse has no physical meaning and is attributed to a slight under- or overestimation of the total capacitance of the ACTFEL stack.

Another interesting phenomenon regarding the charge transfer inside the phosphor is the rate at which charge is transferred. In the ALE sample a larger amount of charge is transferred during the beginning of the field-control pulse and less towards the end of the pulse. For the sputtered sample the rate of the transfer of charge is constant throughout the application of the field-control pulse. A definitive explanation cannot be given until further research is done. Studying the charge transfer rate versus sample temperature could provide helpful data.

The reason for the increase in conduction charge with increasing temperature also needs to be investigated. The reduction of charge at low temperature is believed due to

the reduction of optical phonons, and hence a reduction in phonon-assisted tunneling, as well as the possibility of carriers being trapped in deep traps.

The increase in luminescence at low temperature for the ALE sample is believed to be due to a combination of a decrease in optical phonon scattering and a decrease in the nonradiative transition rates. With the decrease of the vibrational energy of the lattice at low temperature, electrons undergo fewer collisions and therefore gain higher energies in the applied phosphor field. As the electron strikes the luminescent impurity, more energy is transferred to the ion, and subsequently the ion is excited into a higher energy level. For a given energy level, a decrease in its nonradiative decay rate results in a decrease in the overall decay rate and a larger emission.

For the sputtered sample, the luminescence decreases with lower temperature. The only ways to lower the luminescence are to have fewer conduction electrons, to have "cooler" conduction electrons, or to have a decrease in overall effective decay rate. Lowering the temperature "cools" the lattice by decreasing the phonon density. This should decrease scattering and cause a "hotter" distribution of conduction electrons, not a "cooler" distribution. The radiative decay rate is given by the Einstein A coefficient and is temperature independent. Lowering the temperature could decrease the nonradiative coupling between levels. If nonradiative decay is a competing process in the same transition, then the luminescence should increase as temperature decreases. If, however, a nonradiative process is filling the upper state, then lowering the temperature could lower the luminescence.

Using Krupka's ratio of 5D_3 to 5D_4 peak intensities on the field-control spectra shows no clear saturation trends. As with the regular pulse case, using this analysis at higher temperatures where nonradiative transitions are present gives no easily interpreted results. One clear fact is that the ALE device ratios are always a factor of 2.5 to 3 times larger than for the sputtered samples, both at room- and low temperature. This means that the upper energy levels are being more efficiently populated in the ALE material. This

could be due to less nonradiative decay of the 5D_3 to 5D_4 transition or to a greater fraction of electrons exciting Tb^{3+} to the 5D_3 or higher states.

Finally, if the conduction electrons come from the interface states via a thermally-assisted tunneling process, then lowering the temperature would decrease the number of conduction electrons. So the decrease in luminescence at lower temperature in the sputtered sample is phonon-related and could be due to poorer electron emission from the interface states or from a decrease in nonradiative filling of the upper luminescent level. Studying excitation and de-excitation spectra of the sputtered ZnS:TbOF will provide more information on nonradiative and radiative transition rates, and could resolve this puzzle.

It is seen that the experimental results agree qualitatively with the Monte Carlo simulations. An increase in quantum yield is observed, both for low- and room temperature. For the ALE sample, saturation of the quantum yield is observed. This is in agreement with the Monte Carlo simulation, although the onset occurs at different fields. For the sputtered sample, saturation cannot be identified at room temperature, because large enough fields are not attained. Saturation can be observed at low temperature, however, where higher fields are possible.

The increase in quantum yield shows that the number of excitations per injected electron increases with increasing fields. Saturation occurs because band-to-band impact ionization effectively reduces the number of electrons contributing to luminescence at large phosphor fields. Band-to band ionization occurs when a hot electron ($E > 4.3$ eV) strikes an electron in the valence band. That electron receives enough energy to reach the conduction band. A mobile hole is left in the valence band.

When comparing the quantum yield of the ALE and the sputtered sample (see Fig. 4-36), it is noticed that the efficiency of the sputtered sample changes little with temperature. It seems almost temperature independent. The ALE sample, however, exhibits a large increase in efficiency at lower temperature. At room temperature the

efficiency of the ALE sample is much worse than the sputtered sample. This shows that for the ALE sample a mechanism exists that is temperature dependent and greatly affects the efficiency of the EL device. The ALE device differs from the sputtered device in many respects. The ALE insulators are ATO instead of BTO. As high quality insulators they are excellent, but they may also have much different interface properties. The Tb doping in the ALE material is put in monolayer planes during growth. In the sputtered material the dopant is a TbOF group of atoms and is distributed throughout the phosphor. It is important to find the cause for this temperature dependent efficiency in ALE samples since only a possible increase in efficiency at room temperature will benefit current EL display devices.

5.0 Conclusions and Recommendations for Future Work

5.1 Conclusions

There are three main conclusions to be made from this work. First, the field-control circuit along with the period of 10 kHz regular pulses between field-control pulses does indeed provide a fixed, steady-state "pre-field-control" condition and constant field within the phosphor layer.

Second, the approach to assess the hot electron energy distribution, suggested by Krupka [8], is found not to be accurate at higher temperatures with considerable phonon densities because nonradiative transitions are not accounted for. Nonradiative transitions are due to phonons and it is necessary to operate at very low temperatures to minimize these nonradiative transitions. Room temperature data is therefore not accurate in terms of the hot electron energy distribution, information inferred from the intensity ratios.

Third, the normalized Tb impact excitation quantum yield is shown to be a powerful tool for analyzing and optimizing the efficiency of phosphors. By dividing the luminescent intensity by the total number of transferred conduction electrons, the luminous efficiency per electron is found. This is the critical value in comparing phosphor materials and device operation.

5.2 Future Work

The questions raised in interpreting the results of this work provide many topics for further study. Below are listed some of the more urgent ones.

1) Determination of the nonradiative (and radiative) transition rates in ZnS:Tb and ZnS:TbOF

In order to accurately measure the hot electron distribution in ZnS:Tb at room temperature, it is necessary to know the effects of nonradiative transitions on the luminescent signals. A more thorough understanding of radiative and nonradiative transitions can be obtained by studying the excitation and de-excitation decay time constants at various fields and temperatures. By cooling the devices to less than 50 K, most of the nonradiative transitions can be eliminated. The remaining decay rate is the radiative rate. As the temperature is raised, the nonradiative effects will reappear. Hopefully, it will be possible to sort out nonradiative filling of the upper levels from emptying these levels through competition with radiative decay. Temperature dependent measurements will provide more information on the extent of nonradiative transitions in both ALE and sputtered samples. With this knowledge it is possible to improve the ALE sample in order to obtain a better efficiency at room temperature.

2) Measurement of normalized optical yield on other phosphors such as ZnS:Mn, CaGaS:Ce, and SrS:Ce, and comparison with models

The determination of the normalized optical yield, i.e. the luminescence per conduction electron as a function of phosphor field provides data for device optimization. The ZnS:Mn phosphor should show output at much lower fields. This should allow more light out before the efficiency saturates due to band-to-band impact ionization of the ZnS. The extension of current transport simulations to this system to compare with experiments will be interesting. All the other phosphor systems need to also have their normalized efficiencies determined.

3) Tunneling mechanisms at room and low temperature

More experimental work is needed in determining which tunneling mechanism is dominant at room and low temperature. At room temperature more carriers are present in the phosphor. The origin of all these carriers is still not solved. The carriers can come from interface states alone, or some of them are generated in the bulk. At low temperature less carriers are present and are believed to come from interface states. Again, temperature studies can help identify phonon-assisted tunneling effects on the conduction current. More work in this area might provide information on the presence of space charge, as well as the source of additional carriers at room temperature.

4) Dependence of the conduction carrier density on the pulse length and height of the field-control pulse

It has been noticed that much more charge is extracted from interface states using the field-control pulse than using regular trapezoidal pulses. The main difference between the two pulses is the length of the field-control pulse. The length was set to $400\mu\text{s}$, which is ten times longer than the standard pulse. This increase in time allows the phosphor field to extract more charge from interface states. Hence, the polarization charge increases. More research in this area is recommended in determining whether all charges come from interface states or if some of the charge originates in the bulk.

5) Comparison of sputtered samples using ATO and BTO insulators

A study of the effects of these two insulators can provide the reason for the current fluctuations in voltage and phosphor field taking place at room temperature under the application of a field-control pulse. It is proposed that the poorer quality of the BTO insulators in the sputtered samples results in micro breakdowns of the phosphor layer causing the instability at higher fields. Substituting ATO for the BTO could clarify this.

6) Refinement of the current field-control circuit

The present field-control circuit uses standard LM741 op-amps which are fairly slow devices. Initially, some video bandwidth op-amps with fast voltage slew rates were used but trouble with voltage offsets were encountered. Testing of the rise time limits of the field-control circuit is needed with, perhaps, the use of faster op-amps. The RC time constant also needs to be carefully determined and modified to allow very short, fast pulses to be applied for optical excitation/de-excitation experiments.

Bibliography

- [1] C. B. Sawyer and C. H. Tower, *Phys. Rev.*, number 35, pp. 269, 1930.
- [2] R. C. Arthur, J. D. Davidson, J. F. Wager, I. Khormaei, and C. N. King, "Capacitance-voltage characteristics of alternating-current thin film electroluminescent devices", *Appl. Phys. Lett.*, volume 56, pp. 1889, 1990.
- [3] J. D. Davidson, J. F. Wager, I. Khormaei, C. N. King, and R. Williams, "Electrical characterization and modeling of alternating-current thin film electroluminescent devices", *IEEE Trans. on Elect. Dev.*, volume 39, number 5, pp. 1122, 1992.
- [4] J. D. Davidson, M.S. thesis, Oregon State University, 1991.
- [5] S. M. Sze, *Physics of semiconductor devices*, 2nd ed., Wiley, New York, pp. 49-51, 1981.
- [6] A. A. Douglas, M.S. thesis, Oregon State University, 1993.
- [7] A. Abu-Dayah, S. Kobayashi, and J. Wager, "Internal charge-phosphor field characteristics of alternating-current thin film electroluminescent devices", *Appl. Phys. Lett.*, volume 62, number 7, pp. 744-746, 15 February 1993.
- [8] D. C. Krupka, "Hot-electron impact excitation of Tb^{3+} luminescence in $ZnS:Tb^{3+}$ thin films", *J. Appl. Phys.*, volume 43, number 2, pp. 476-481, February 1972.
- [9] K. Brennan, "Theory of high-field electronic transport in bulk ZnS and ZnSe", *J. Appl. Phys.*, volume 64, number 8, pp. 4024-4030, 15 October 1988.
- [10] K. Bhattacharyya, S. M. Goodnick, and J. F. Wager, "Monte Carlo simulation of electron transport in alternating-current thin-film electroluminescent devices", *J. Appl. Phys.*, volume 73, number 7, pp. 3390-3395, 1 April 1992.
- [11] S. Pennathur, personal communication.
- [12] H. J. Fitting, A. Von Czarnowski, and G. O. Mueller, "Ballistic transport in alkaline earth sulfides", *J. Crystal Growth*, volume 101, pp. 876-881, 1990.
- [13] R. Mach and G. O. Mueller, "Ballistic transport and electroluminescence in IIB-VI and IIA-VI compounds", *J. Crystal Growth*, volume 101, pp. 967-975, 1990.

- [14] D. E. Gray, *American Institute of Physics Handbook*, McGraw-Hill, p. 7-39, 1963.
- [15] G. Herzberg and J. Spinks, "*Atomic spectra and atomic structure*", Dover Publications, 1944.
- [16] L. G. Van Uitert and L. F. Johnson, "Energy transfer between rare-earth ions", *Journ. of Chem. Phys.*, volume 44, number 9, pp. 3514-3522, 1 May 1966.
- [17] L. A. Riseberg and H. W. Moss, "Multiphonon orbit-relaxation in LaBr_3 , LaCl_3 , and LaF_3 ", *Phys. Rev. Lett.*, volume 19, number 25, pp. 1423-1426, 18 December 1967.
- [18] A. S. Marfunin, "*Physics of minerals and inorganic materials*", Springer Verlag, pp. 1-44, 1979.
- [19] K. S. Thomas, S. Singh, and G. H. Dieke, "Energy levels of Tb^{3+} in LaCl_3 and other chlorides", *J. Chem. Phys.*, volume 38, number 9, pp. 2180-2190, 1 May 1963.
- [20] D. C. Krupka and D. M. Mahoney, "Electroluminescence and photoluminescence of thin films of ZnS doped with rare-earth metals", *J. Appl. Phys.*, volume 43, number 5, pp. 2314-2320, May 1972.
- [21] S. Tanaka, H. Kobayashi, and H. Sasakura, "Evidence for the direct impact excitation of Mn centers in electroluminescent ZnS:Mn films", *J. Appl. Phys.*, volume 47, number 12, pp. 5391-5393, December 1976.
- [22] A. Mikami, T. Ogura, K. Taniguchi, M. Yoshida, and S. Nakajima, "Excitation processes of the Tb center in a ZnS:Tb,F thin-film electroluminescent device", *J. Appl. Phys.*, volume 64, number 7, pp. 3650-3657, 1 October 1988.
- [23] E. Bringuier, "Impact excitation in ZnS-type electroluminescence", *J. Appl. Phys.*, volume 70, number 8, pp. 4505-4512, October 1991.
- [24] A. A. Douglas, J. F. Wager, K. Battacharyya, S. M. Goodnick, D. C. Morton, J. B. Koh, and C. P. Hough, "Hot-electron Luminescence in ZnS ACTFEL Devices", *SID 93 Digest*, pp. 851-854, 1993.
- [25] A. I. Abu-Dayah, M.S. Thesis, Oregon State University, 1993.